Photochemistry of Methane and Ethane in the Martian Atmosphere

Citation for published version:
Taysum, BM & Palmer, PI 2020, 'Photochemistry of Methane and Ethane in the Martian Atmosphere', *Journal of Geophysical Research: Planets*, vol. 125, no. 6. https://doi.org/10.1029/2020JE006491

Digital Object Identifier (DOI):
10.1029/2020JE006491

Link:
Link to publication record in Edinburgh Research Explorer

Document Version:
Publisher's PDF, also known as Version of record

Published In:
Journal of Geophysical Research: Planets

JGR Planets

RESEARCH ARTICLE
10.1029/2020JE006491

Key Points:

- Formaldehyde and formic acid are two key photochemical products of CH_4 and C_2H_6
- Oxidation of C_2H_6 produces distinct profiles of acetaldehyde
- Photolysis of acetaldehyde, produced by C_2H_6 photochemistry, is a source of atmospheric CH_4

Correspondence to:
B. M. Taysum,
Ben.Taysum@ed.ac.uk

Citation:
Taysum, B. M., & Palmer, P. I. (2020). Photochemistry of methane and ethane in the martian atmosphere. *Journal of Geophysical Research: Planets*, *125*, e2020JE006491. https://doi.org/10.1029/2020JE006491

Received 20 APR 2020
Accepted 25 MAY 2020
Accepted article online 10 JUNE 2020

Photochemistry of Methane and Ethane in the Martian Atmosphere

Benjamin M. Taysum[1,2] **and Paul I. Palmer**[1,2]

[1]School of GeoSciences, University of Edinburgh, Edinburgh, UK, [2]Centre for Exoplanet Science, University of Edinburgh, Edinburgh, UK

Abstract We develop an existing 1-D photochemistry model to include a comprehensive description of organic chemistry on Mars that includes the oxidation products of methane (CH_4) and ethane (C_2H_6),a longer-chain hydrocarbon that can be used to differentiate between abiotic and biotic surface releases of CH_4. We find that CH_4 is most volatile between 20 and 50 km during Mars' northern summer, where the local atmospheric CH_4 lifetime lowers to 25–60 years. We study atmospheric formaldehyde (HCHO) and formic acid (HCOOH), as the two common oxidation products of CH_4 and C_2H_6, and acetaldehyde (CH_3CHO) and acetic acid (CH_3COOH) as unique products of C_2H_6. We focus our analysis of these gases at Mars' aphelion and perihelion at latitudes between -30° and 30°, altitudes from the surface to 70 km, and from a homogeonous initial condition of 50 pptv of CH_4 and C_2H_6. From this initial condition, CH_4 produces HCHO in a latitude-independent layered structure centered at 20–30 km at aphelion with column-averaged mixing ratios of 10^{-4} pptv, and oxidation of C_2H_6 produces HCHO at 10^{-2} pptv. Formic acid has an atmospheric lifetime spanning 1–10 sols below 10 km that shows little temporal or zonal variability and is produced in comparable abundances (10^{-5} pptv) by the oxidation of C_2H_6 and CH_4. We also find that oxidation of 50 pptv of C_2H_6 results in 10^{-3} pptv of CH_3CHO and 10^{-4} pptv of CH_3COOH. Subsequent UV photolysis of this CH_3CHO results in 10^{-4} pptv of atmospheric CH_4, potentially representing a new atmospheric source of Martian CH_4.

Plain Language Summary Reports of atmospheric methane (CH_4) on Mars, a potential biosignature, have been made via ground-based telescopes, the Mars Express orbiter, and the Curiosity Rover. However, atmospheric CH_4 has been not observed by all instruments, including the recently launched ExoMars Trace Gas Orbiter. Reconciling these different measurements of the Martian atmosphere with photochemical model calculations remains a challenge, implying that models are missing a CH_4 loss process, and/or there are uncharacterized errors in the data. Here, we use a photochemical model of CH_4 and ethane (C_2H_6) and their oxidation products, many of which can now be observed from orbiting satellites, to help reconcile models and data. Using this model, we show that UV photolysis of acetaldehyde, an oxidation product of C_2H_6, is a small but potentially significant source of atmospheric CH_4.

1. Introduction

There is considerable debate in the community about the validity and robustness of detections of atmospheric methane (CH_4) on Mars. Detections and nondetections of atmospheric CH_4 have been reported using data collected by satellites (Formisano et al., 2004; Fonti & Marzo, 2010; Geminale et al., 2008, 2011; Giuranna et al., 2019), Earth-based telescopes (Krasnopolsky, 2007, 2011, 2012; Krasnopolsky et al., 1997, 2004; Mumma et al., 2009; Villanueva et al., 2013), and in situ instruments (Moores et al., 2019; Webster et al., 2015, 2018). This debate highlights the difficulty of measuring atmospheric CH_4 on Mars and the gaps in our current understanding of the production and loss terms that determine atmospheric CH_4 on Mars. We explore how the presence of CH_4 could be determined by its oxidation products and in the process discuss how abiotic CH_4 could be potentially produced by organic chemistry.

Detections of atmospheric CH_4 at the Gale crater by the NASA Curiosity Rover were observed episodically rising from mean volume mixing ratios (VMRs) of 0.69 ± 0.25 parts per billion (ppbv) to 7.20 ± 2.10 ppbv across a 60-sol period (Webster et al., 2015). The diurnal variations of CH_4 observations via Curiosity have recently been substantiated by the ExoMars Trace Gas Orbiter's Nadir and Occultation for Mars Discovery (NOMAD) spectrometer and Atmospheric Chemistry Suite (ACS) (Korablev et al., 2019; Moores et al., 2019). These recent measurements by NOMAD and ACS constrain the upper limit of CH_4 in the Martian atmosphere to 0.05 ppbv.

Ground-based telescopes reported a signal of a plume that contained approximately 19,000 tonnes of CH_4 (Mumma et al., 2009) near the Syrtis Major region during Mars' northern hemisphere's midsummer, consistent with an estimated 0.60 kg $m^{-2}s^{-1}$ seasonal point source of organic compounds. Other searches for CH_4 on Mars have conversely failed to detect the compound (Webster et al., 2013), including the Trace Gas Orbiter's year and a half long search (Korablev et al., 2019). This highlights the possibility of methane being significantly more temporally variable than current models predict (Lefèvre & Forget, 2009). This inconsistency with regard to CH_4's detection has also ignited some polemic against the existance of the gas on Mars (Zahnle et al., 2011). Recent analysis of data from the Planetary Fourier Spectrometer (PFS) aboard the Mars Express orbiter identified the presence of CH_4 in the Martian atmosphere that was confirmed via independent observations by Giuranna et al. (2019). These results appear to confirm Curiosity's detection of CH_4 at the Gale Crater. The team retrieved column integrated VMRs of 15.5 ± 2.50 ppbv above the Gale Crater only 1 Martian day (sol) after the Curiosity rover's measurement of a 5.78 ± 2.27 ppbv (Webster et al., 2015).

To further study these possible emissions of CH_4 and to also provide a more detailed series of observations of the vertical structure and composition of Mars' atmosphere, the ExoMars mission program was established by the European Space Agency (ESA) (Vago et al., 2015) and the Russian Roscosmos State Corporation for Space Activities. The first mission conducted within this program was the launch of the Trace Gas Orbiter (TGO) in 2016 that included two suites of spectrometers, the Nadir and Occultation for MArs Discovery (NOMAD) spectrometer (Vandaele et al., 2018) and the Atmospheric Chemistry Suite (ACS) (Korablev et al., 2017). The TGO underwent 11 months of aerobraking to reduce its orbital speed and altitude, eventually establishing an approximately circular orbit of altitude roughly 400 km allowing scientific observations to start in April 2018 (Vandaele et al., 2019). Over the first year, no successful observations of CH_4 were reported by the TGO instrumentation (Korablev et al., 2019). We developed our investigation bearing in mind the capabilities of TGO instruments, especially the solar occultation channels of NOMAD (NOMAD-SO) and ACS (ACS-MIR). The NOMAD-SO instrument has been designed to be sensitive to CH_4 abundances as low as 0.025 ppbv when observed in solar occultation mode (Robert et al., 2016). This expected detection limit was compared to the experimental values in (Vandaele et al., 2019). The TGO instruments improved the experimental upper limit of previous instrumentation to reach a limit of roughly 0.05 ppbv for methane. A few profiles reported in Korablev et al. (2019) and obtained via ACS-MIR, measured in clear northern conditions, were able to achieve the most precise detection limits of 0.012 ppbv down to an altitude of roughly 3 km.

Previous studies using 1-D photochemical models (Summers et al., 2002; Wong et al., 2003) calculate the photochemical lifetime of CH_4 to be roughly 300 years below 70 km. In the absence of a strong surface loss process, surface emissions of CH_4 will then become homogeneously distributed across the planet after being introduced into the atmosphere. This inconsistency between models and data means that the available atmospheric data are misinterpreted, and/or there is a loss mechanism that we do no not currently consider in models (Krasnopolsky, 2006). Previous calculations using a global 3-D general circulation model have determined that to reconcile models and data we need a CH_4 loss process that is up to 600 times faster than any known process (Lefèvre & Forget, 2009). That additional sink would lower the atmospheric lifetime of CH_4 from centuries to less than 200 days. With the advent of the TGO, another approach we can take is to analyze observed spatial and temporal variations of the oxidation products of atmospheric CH_4.

In this study, we describe the development of the 1-D photochemistry submodule from the LMD-UK General Circulation Model (GCM) (Forget et al., 1999; Lewis et al., 1999) to include organic chemistry and run it as an independent model to study photochemistry on Mars. We report results from a series of numerical experiments that describe how the presence of CH_4 affects photochemistry on Mars. We also report photochemical results when we replace CH_4 with ethane (C_2H_6) to show this longer-chain hydrocarbon produced richer atmospheric chemistry and allows us to consider an abiotic source of atmospheric CH_4 from the oxidation of acetaldehyde. In the next section we describe our developed 1-D model of Mars photochemistry. In section 3 we report results from our numerical experiments. We conclude the paper in

Table 1
Trace Gas Species Handled by the 1-D PhotoChemistry Submodule

Formula	Name
Inorganic tracers	
CO_2	Carbon dioxide
CO	Carbon monoxide
$O(^1D)$	Atomic oxygen (excited singlet)
$O \equiv O(^3P)$	Atomic oxygen (ground-state)
O_2	Molecular oxygen
O_3	Ozone
H	Atomic hydrogen
OH	Hydroxyl
HO_2	Hydroperoxyl
H_2O_2	Hydrogen peroxide
H_2	Molecular hydrogen
H_2O (vapor and ice)	Water vapor and ice
N_2	Nitrogen
Ar	Argon
Organic tracers (methane oxidation)	
CH_4	Methane
CH_3	Methyl radical
CH_3O_2	Methyl peroxy-radical
CH_3OOH	Methyl hydroperoxide
CH_3OH	Methanol
CH_3O	Methoxide
HCHO	Formaldehyde
HCOOH	Formic acid
$HOCH_2O_2$	Hydromethyl peroxy
$HOCH_2OH$	Methanediol
$HOCH_2OOH$	Hydromethyl hydroperoxide
HCO	Formyl radical
Organic tracers (ethane oxidation)	
C_2H_6	Ethane
C_2H_5	Ethyl radical
$C_2H_5O_2$	Ethyldioxy radical
C_2H_5OOH	Ethyl peroxide
C_2H_5OH	Ethanol
$HOCH_2CH_2O_2$	–
$HOCH_2CH_2O$	–
Ethgly ($(CH_2OH)_2$)	Ethylene glycol
Hyetho2h ($C_2H_6O_3$)	–
CH_3CHO	Acetaldehyde
CH_2CHOH	Ethenol
CH_3CHOHO_2	Hydroxy ethyl peroxy radical
CH_3COOH	Acetic acid
$CH_3CHOHOOH$	–
$CH_3C(O)$	Acetyl radical
$CH_3C(O)OO$	–
$CH_3C(O)OOH$	Peracetic acid
$HCOCH_2O_2$	–
Glyox (OCHCHO)	Glyoxal
HCOCO	–
$HOOCH_2CHO$	Hydroperoxy acetaldehyde
$HOCH_2CHO$	Glycolaldehyde
HOCHCHO	Hydroxyl-vinoxy radical
$HOCH_2CO$	–
$HOCH_2CO_3$	–
$HOCH_2CO_2H$	Glycolic acid
$HCOCO_2H$	–
$HCOCO_3H$	–
$HCOCO_3$	–
$HOCH_2CO_3H$	–

section 4 in which we discuss the implications of our results for broadly understanding atmospheric chemistry on Mars but in particular the implications for detecting the presence of CH_4 and C_2H_6 on Mars using their oxidation products.

2. 1-D Photochemical Model

We use the 1-D photochemistry submodule from the parent 3-D LMD-UK Mars General Circulation Model as the basis for a standalone 1-D model that includes an improved treatment of atmospheric organic photochemistry.

We use this standalone 1-D model to describe time-dependent vertical distributions of trace gases from the surface to an altitude of approximately 70 km, described by 25 vertical layers with a resolution of under 0.5 km below 2 km increasing to a resolution of 10 km above an altitude of 20 km, where 3-D macroscopic processes begin to dominate. We divide a Mars sol into 48 time steps ($\Delta t = 1{,}800$ s), allowing us to describe diurnal variations of trace gases by calculating time-dependent changes in solar zenith angle, taking into consideration changes in solar longitude and axial tilt. To decrease the stiffness of the discretized equations used to compute the photochemical rates of change, determined by a prescribed chemical mechanism described below, we use a chemistry sub-timestep of $\Delta t_c = 600$ s.

Vertical tracer transport between model layers is described by the classical diffusion equation (Mellor & Yamada, 1982). For details on the vertical diffusion and turbulent mixing routines we refer the reader to Forget et al. (1999). We use a radiative transfer scheme (Madeleine et al., 2011) that uses opacity values from the Mars Climate Database v5.3. We describe the condensation and sublimation of carbon dioxide, (Forget et al., 1998), water ice (Navarro et al., 2014), and hydrogen peroxide (H_2O_2), and an implicit chemistry solver computes production and loss rates from photochemical reactions.

2.1. Organic Photochemistry

The 1-D submodel that resides in the LMD-UK MGCM describes the atmospheric chemistry and transport of 15 trace gases: carbon dioxide (CO_2), carbon monoxide (CO), atomic oxygen (O), singlet oxygen ($O(^1D)$), molecular oxygen (O_2), ozone (O_3), hydrogen atom (H), hydroxy radical (OH), hydroperoxyl radical (HO_2), molecular hydrogen (H_2), hydrogen peroxide (H_2O_2), nitrogen (N_2), argon (Ar), and H_2O as ice and vapor. The photochemistry scheme for these compounds consists of 32 chemical reactions (B1) and 10 photolysis reactions (B2).

We build on the chemical mechanism by including 41 new organic compounds, guided by previous studies (Summers et al., 2002; Wong et al., 2003) and also the theoretical measurement capabilities of the NOMAD instrument (Robert et al., 2016), to improve understanding of Mars' atmospheric chemistry. We include CH_4, C_2H_6, and its photochemical products. The extended chemical mechanism represents an additional 106 chemical reactions (B3, B4, B5) and 29 photolysis reactions (B6). A complete list of trace gas species within the 1-D model is provided in Table 1. We present the first analysis of C_2H_6 oxidation products in the Martian atmosphere.

We take the organic chemistry rate coefficients from the CAABA/MECCA v4.0 atmospheric box model (Sander et al., 2019), which is used to model organic chemistry within Earth's atmosphere. We have modified the mechanism to include HCO and C_2H_5 radicals. The CAABA/MECCA v4.0 model neglects these radicals as products and instead includes the products of the radicals with molecular oxygen, O_2. This approximation is sufficient for Earth, where O_2 is present at 21% mass fraction, but on Mars it is present only at a mass fraction of 10^{-3}. Including these radicals allows us to improve the description of organic chemistry. All three-body reaction rate coefficients in the submodule are multiplied by a factor of 2.5, following Nair et al. (1994), to account for the increase in efficiency that CO_2 displays when used as a bath gas in comparison to N_2 or dry air (Kaufman & Kelso, 1967), commonly used in laboratories for the calculation of these coefficients.

To improve the accuracy of the original chemistry routine and to reduce the computational expediency of our chemistry calculation we use a precalculated look-up table to interpolate photolytic frequencies. We calculated these photolysis loss rates using the Tropospheric Ultraviolet and Visible (TUV) Radiation Model (Madronich et al., 2002) that has been adapted for use on Mars (Lefèvre et al., 2004) and using routines to interpolate as function of atmospheric temperature, solar zenith angle, O_3 column density, the total atmospheric column density, the Sun-Mars distance, and the dust opacity. The photolytic reaction j_{HOCH_2OOH} of B6 requires the consideration of the abundance of O_2, as the photolytic product of $HOCH_2OOH$ is the highly reactive $HOCH_2O$ radical. $HOCH_2O$ proceeds to react with molecular oxygen to form HCOOH and OH. To limit the number of compounds that the steady-state approximation has to be applied to, the 1-D model multiplies the photolytic frequency extracted from the TUV look-up table by a temperature independent factor of 3.50×10^{-14} (Veyret et al., 1982) and the number density of O_2 at the respective layer.

To improve the accuracy of the original chemistry routine and to reduce the stiffness of the chemistry calculations, we decreased the chemical timestep to 600 seconds. This has the additional benefit of allowing the Semi-Implicit Backward Euler Method (SIBEM) to be used for a larger number of species across timestep Δt_c while conserving mass of the studied tracers. For species with photochemical lifetimes shorter than 100 seconds we consider a family of species, for example, odd-hydrogen (HO_x) and odd-oxygen (O_x) families, which have a collective lifetime longer than the timestep. We handle these compounds, H, OH, HO_2, and $O(^1D)$, $O(^3P)$, O_3, respectively, via the assumption of photochemical equilibrium (Rodrigo et al., 1990). The routine calculates dimensionless partition functions of the loss rates of H/HO_2, OH/HO_2, and $O(^3P)/O_3$ (s^{-1}/s^{-1}) and sums the abundances of each family, HO_x and O_x, which possess atmospheric lifetimes greater than that of the chemistry timestep, allowing them to be computed via the SIBEM equation. The partition functions are then applied to compute each individual compounds respective abundance.

2.2. Time-Dependent Meteorological Boundary Conditions

To drive the 1-D photochemistry model, we use time-dependent lateral atmospheric boundary conditions of temperature, wind, water vapor volume mixing ratios, and surface pressure from the Mars Climate Database v5.3 (MCD) (Millour et al., 2017). We interpolate the 3-D meteorological fields from the MCD data set, taking into account latitude, solar longitude, and local time.

All interpolated values from the MCD data set are longitudinal means, calculated independently by ourselves, acknowledging that there are only small longitudinal variations of meteorological parameters that are due primarily to topographical features. We take advantage of this so that the horizonal footprint of our model is representative of a zonal band of 3.75° in latitude, which is the latitudinal resolution of the MCD dataset. Zonal and meridional transport is not accounted for by the 1-D model. We use an interpolation routine for trace gases that have atmospheric chemistry lifetimes greater than the e-folding residence times associated with meridional advection of trace gases out of the zonal band, which is approximately 0.5–2 sols. We use this approach to drive the model with vertical profiles of CO_2, CO, O_2, H_2, and water vapor, ensuring the photochemical environment is consistent with the meteorological fields from the MCD, allowing the 1-D model to be accurately representative of the temporally and spatially variable oxidising environment. Seasonal water vapor profiles from MCD are especially important for the 1-D photochemical calculations as the photolysis of Martian H_2O is the source of the highly reactive odd-hydrogen species, $HO_x = H + OH + HO_2$, which help drive the oxidation of organic species and O_3 chemistry (Lefèvre et al., 2004).

The overarching purpose of using these boundary conditions is that we can describe detailed 1-D atmospheric chemistry, including diurnal and seasonal changes associated with Mars' atmosphere, without the computational overhead of solving the 3-D dynamical equations. In particular, the boundary conditions help to maintain realistic values and variations of wind profiles that underpin vertical diffusion calculations that correspond to calculating vertical transport. For all of our calculations, we use a prescribed dust scenario produced from the assimilation of observations of the dust optical depth made by the Mars Global Surveyor's Thermal Emission Spectrometer (Montabone et al., 2015) during Mars Year (MY) 24. This scenario is regarded as a "best guess" of the mean annual dust variability experienced on Mars without the presence of global or significant regional dust storms. The 1-D photochemical model is capable of operating in dust-storm scenarios using data from the MCD v5.3, but these calculations are beyond the scope of the current study.

We limit our calculations to latitudes less than 30°, where most recent observations of CH_4 on Mars have been reported (Mumma et al., 2009; Webster et al., 2015, 2018). At latitudes higher than 40° in both hemispheres, the MCD boundary conditions also allow us to describe the large-scale seasonal changes in atmospheric temperature that result from condensation, deposition, and sublimation of CO_2, which produce significant changes in surface pressure. However, at these latitudes meridional wind profiles above the planetary boundary layer can become large enough to lower the tracer e-folding timescales to values too small for the 1-D model to neglect while still producing reliable model results. At latitudes less than 30°, the 1-D model in this work can be used to produce time-dependent tracer profiles for periods limited to 2 sols.

2.3. Definition of Numerical Experiments

We use the 1-D model to determine vertical profiles of organic compounds that evolve from a hypothetically fixed and vertically uniform 50 pptv profile of CH_4. We have chosen this value because it is consistent with the upper limit of Martian CH_4 determined by data collected from the ACS/NOMAD instruments aboard the TGO (Korablev et al., 2019).

For this calculation, we initialize the model 10 sols prior to the point where solar longitude $L_S = 0°$ with initial meteorological conditions and tracer profiles of CO_2, CO, O_2, water vapor, and H_2 from the previously detailed MCD v5.3 look-up table and 10 ppbv of CH_4 distributed evenly across all 25 atmospheric layers ranging from the surface to approximately 70 km. We then run the 1-D over one Mars year, 668 sols, following a 10-sol spin-up period, taking into account diurnal and seasonal (orbital) variations in solar zenith angle and corresponding changes in solar flux and photolytic frequencies. We report calculations at latitudes of 30° N, 2.5° N, and 30° S to investigate possible spatial variations in organic product profiles.

Following this investigation into the annual variations of the products produced by the steady and homogeneous CH_4 background, we use the 1-D model to investigate time-dependent photochemical processes that result from oxidation of CH_4 and C_2H_6. For these experiments, we initialize the 1-D model at the required latitude and solar longitude at 00:00 local time (LT) with 0 pptv CH_4 and other non-methane organic compounds. We use a five-day spin-up period at a constant solar longitude when we use trace gas profiles of CO_2, CO, O_2, H_2, and water vapor from the MCD v5.3 (section 2.2) and diurnally varying atmospheric parameters. This spin-up enables the HO_x and O_x chemistry to partition to the solar-longitude environment. After five sols, we add a vertically uniform 50 pptv profile of CH_4 at 00:00 LT. We then let the model run freely for one further sol, and present the photochemical products at a local time of 18:00 LT when solar occultation measurements are typically collected. We adopt a similar approach to examine the photochemistry of C_2H_6.

3. Results

We use the 1-D model described in the previous section to understand the seasonal chemical composition of the Martian atmosphere as a function of latitude that corresponds to a fixed, uniform vertical distribution of atmospheric CH_4. We present a similar set of calculations that correspond to a uniform vertical distribution of atmospheric C_2H_6.

3.1. Methane Oxidation in the Atmosphere of Mars

Figure 1 describes the initial photochemical oxidation steps of atmospheric CH_4 on Mars. The dominant atmospheric losses of CH_4 are oxidation by the hydroxyl radical (OH) and the excited singlet oxygen

($O(^1D)$) and photolysis. The loss rates for atmospheric CH_4 vary as a function of solar longitude. There are a number of high-yield oxidation products that are produced rapidly, potentially allowing us to colocate elevated values with CH_4 emissions and that are observable from orbiting instruments. In this paper we will restrict our analysis to the production of formaldehyde (HCHO) and formic acid (HCOOH).

Figure 2 shows an illustrative vertical distribution of CH_4 loss factors (s^{-1}) at the solar longitudes of 71° and 271°, times at which Mars' orbit is furthest from and closest to the Sun, respectively. Loss factors, units of s^{-1}, are distinguished from loss rates, units of molec $cm^{-3}s^{-1}$, as loss factors provide a better insight into the reactivity of the surrounding environment. These values after being multiplied by CH_4 number densities equate to the rate of photochemical loss of CH_4 (molec $cm^{-3}s^{-1}$), that is, the loss rate.

From the Martian surface to the top of the Martian hygropause, approximately 10 km at L_S 71° and 45 km at L_S 251°, the dominant loss process for CH_4 is from oxidation by OH. Consequently, at these altitudes the rate of OH production, driven by the photolysis of water vapor, are larger than outside this altitude range. Above these altitudes, the abundance of $O(^1D)$ increases, reflecting the drop in its loss from reaction with water vapor. Between the top of the hygropause and roughly 60 km, $O(^1D)$ becomes the dominant loss of atmospheric CH_4. There are three oxidation channels associated with this reaction (B4), the most efficient producing CH_3 and OH. Photolysis of CH_4 becomes significant only at altitudes higher than 60 km. The decreasing abundance of $O(^1D)$ atoms in the upper atmosphere results in a small vertical region, 50–60 km, where CH_4 loss rates decline before photolysis becomes important at higher altitudes. Below 60 km, the effect of UV radiation on CH_4 is negligible, and photochemical contributions made by methyl radical isotopologues can be disregarded. This highlights that the primary atmospheric sinks of CH_4 change seasonally, with $O(^1D)$ dominating in the aphelion seasons and OH dominating in the perihelion. The stronger reaction rates of $O(^1D)$ with CH_4 can thus be expected to produce greater abundances of potentially observable organic species within the aphelion seasons of Mars.

The local atmospheric lifetime of CH_4, incorporating all chemical loss terms (Figure 2), varies as a function of latitude and solar longitude. Differences between latitudes are determined by the solar radiation being received, which is a function of solar longitude and Mars' obliquity. Local atmospheric lifetimes range from 25 to 1,700 years (Appendix A0.1). These values, with a significant and localized surface loss process, would generate a large, slowly varying background value for CH_4 that would be difficult to attribute to individual surface sources. Local atmospheric lifetimes reach a minimum of 25–200 years between the top of the hygropause and approximately 50 km due to the larger abundance of the $O(^1D)$ atom. Below the hygropause where OH is the dominant sink, local atmospheric lifetimes vary between 200 and 425 years. The longest local lifetimes of 1,000–1,700 years lie between 50 and 60 km during winter ($L_S = 270–360°$), as described above, where the OH and $O(^1D)$ loss processes decline and before photolysis dominates above 60 km.

These local atmospheric photochemical lifetimes are significantly longer than the corresponding atmospheric transport timescales across all altitudes and solar longitudes. We study the variance of these local photochemical lifetimes with solar longitude, altitude, and Mars latitude to understand where are the most photochemically active regions for CH_4 (and below for C_2H_6) and consequently where we expect the largest production rates for their oxidation products. Calculating the vertically integrated photochemical lifetime of CH_4 with the 1-D model (Appendix A0.1) yields timescales that correspond well to those calculated in previous studies (Krasnopolsky et al., 2004; Lefèvre & Forget, 2009; Summers et al., 2002), with the 1-D model producing values ranging between 250 and 550 terrestrial years across the latitude ranges studied here of 30° south to 30° north.

Figure 3 shows vertical profiles of the volume mixing ratios of organic compounds, radicals, peroxy-radicals, and long-lived species from left to right that result from the oxidation of a fixed, uniformly distribution 50 pptv of atmospheric CH_4. For this calculation we initialize the 1-D model with 0 pptv of CH_4 across all vertical layers at $L_S = 71°$ and $L_S = 251°$, 00:00 LT, at a latitude of 2.5°, the latitude at which a CH_4 plume has been previously observed (Mumma et al., 2009). We spin-up for five sols using detailed MCD v5.3 tracer profiles (section 2). We then insert a fixed, uniform profile of 50 pptv of CH_4 into the model and run forward for one sol. We sample the model at 18:00 LT on sol 6, allowing sufficient time (18 hours) for products to be produced but a short enough time to ensure these products are not advected out of the column. This allows us to study the resulting CH_4 oxidation product concentrations. We show values for CH_4, HCHO, HCOOH,

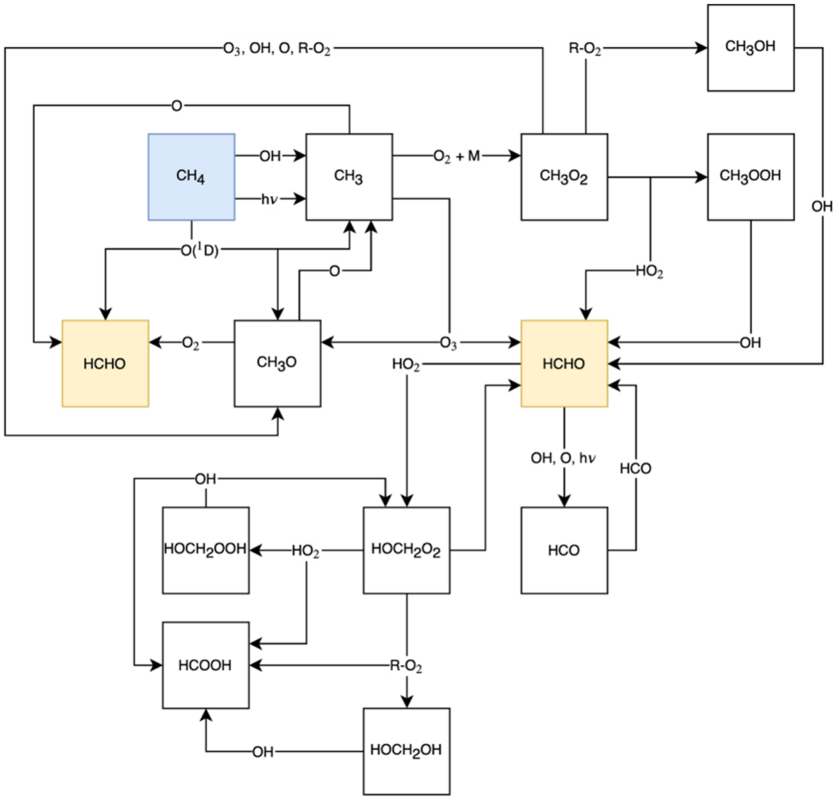

Figure 1. Primary stages of the CH_4 photochemistry that we use in our 1-D photochemistry model, taken from the CAABA/MECCA v4.0 chemical mechanism.

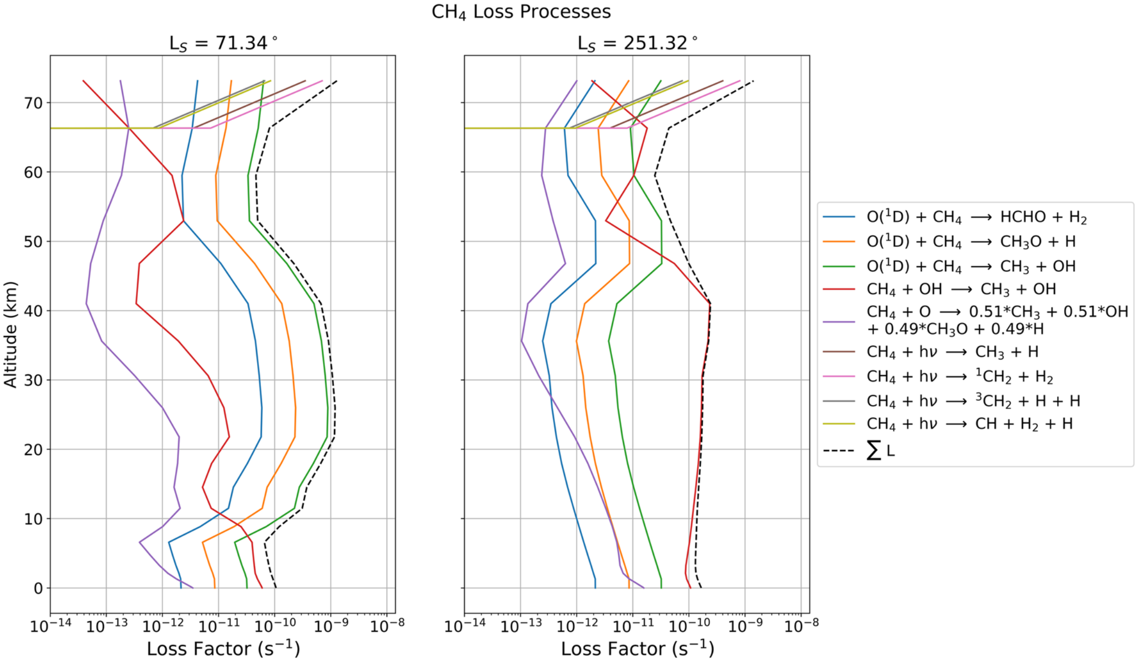

Figure 2. Photochemical loss factors (s^{-1}) CH_4 in our 1-D photochemistry model at latitude 2.5° N, local time 12:00, and solar longitudes 71° and 251° (Mars' aphelion and perihelion, respectively) as a function of altitude.

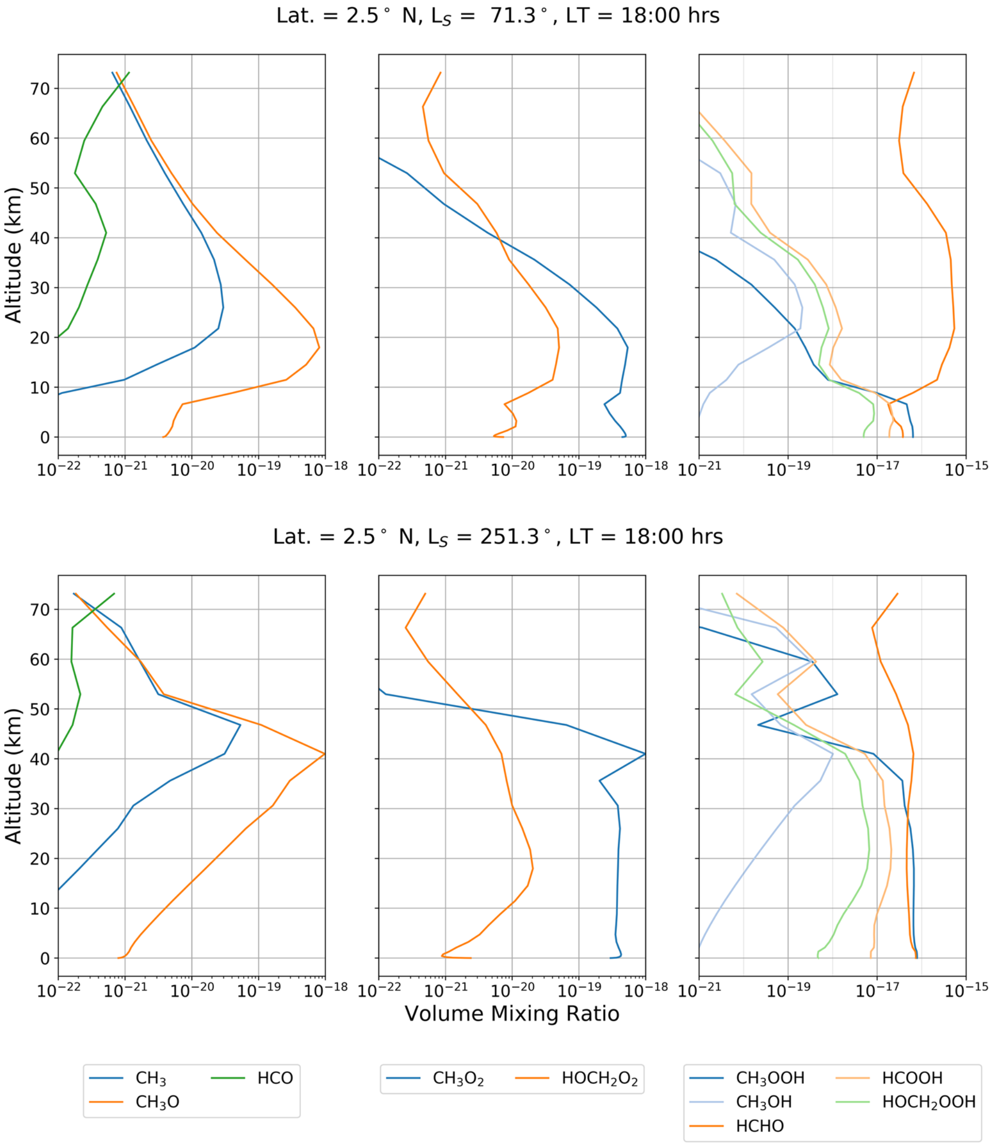

Figure 3. Volume mixing ratio profiles of major photochemical products of 50 pptv of CH_4 after one sol. These include formaldehyde (HCHO), formic acid (HCOOH), methanol (CH_3OH), methyl hydroperoxide (CH_3OOH), hydromethyl peroxy ($HOCH_2O_2$), and hydromethyl hydroperoxide ($HOCH_2OOH$).

methanol, methyl hydroperoxide (CH_3OOH), hydromethyl peroxy ($HOCH_2O_2$), and hydromethyl hydroperoxide ($HOCH_2OOH$). The two products with the highest photochemical yields are HCHO and HCOOH. We find that HCHO has column averaged mixing ratios of 5.43×10^{-16} and 7.41×10^{-17} molecule/molecule at $L_S = 71°$ and 251°, respectively. HCOOH has a column averaged mixing ratio of 2.31×10^{-17} and 2.08×10^{-17} molecule/molecule at $L_S = 71°$ and 251°, respectively. We describe below the responsible production and loss rates associated with these two compounds.

Production rates of methanol are small in our 1-D model, which is driven by a realistic 50 pptv of CH_4. Previous studies that have used a much larger 100 ppmv profile of CH_4 (e.g., Wong et al., 2003) have still struggled to produce Martian methanol above pptv values. CH_3OH has prominent features at IR wavelengths, making it a valuable observed species to help constrain our understanding of organic chemistry. Our 1-D model calculates CH_3OH column average mixing ratios of 2.09×10^{-19} and 1.01×10^{-18} molecule/molecule at $L_S = 71°$ and 251°, respectively. These small quantities are due to the two main production terms for CH_3OH (Table B4) involving CH_3O_2 and CH_3 radicals that are not produced in large quantities by 50 pptv of CH_4. Consequently, we will only discuss CH_3OH in context of HCHO and HCOOH.

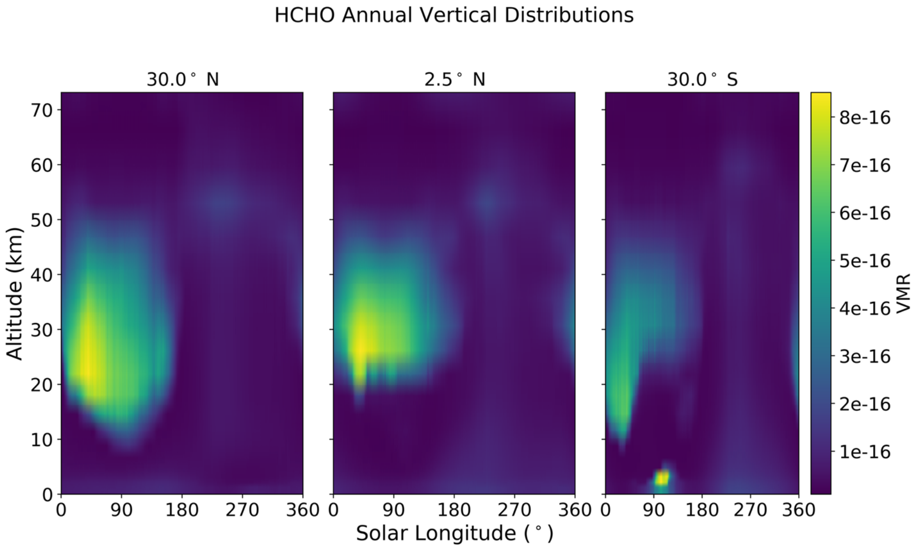

Figure 4. Vertical profiles of HCHO (pptv) from the photochemistry of 50 pptv CH_4 within a zonal band centered on latitudes 30° N, 2.5° N, and 30° S, across all solar longitudes, as calculated by our 1-D photochemical model.

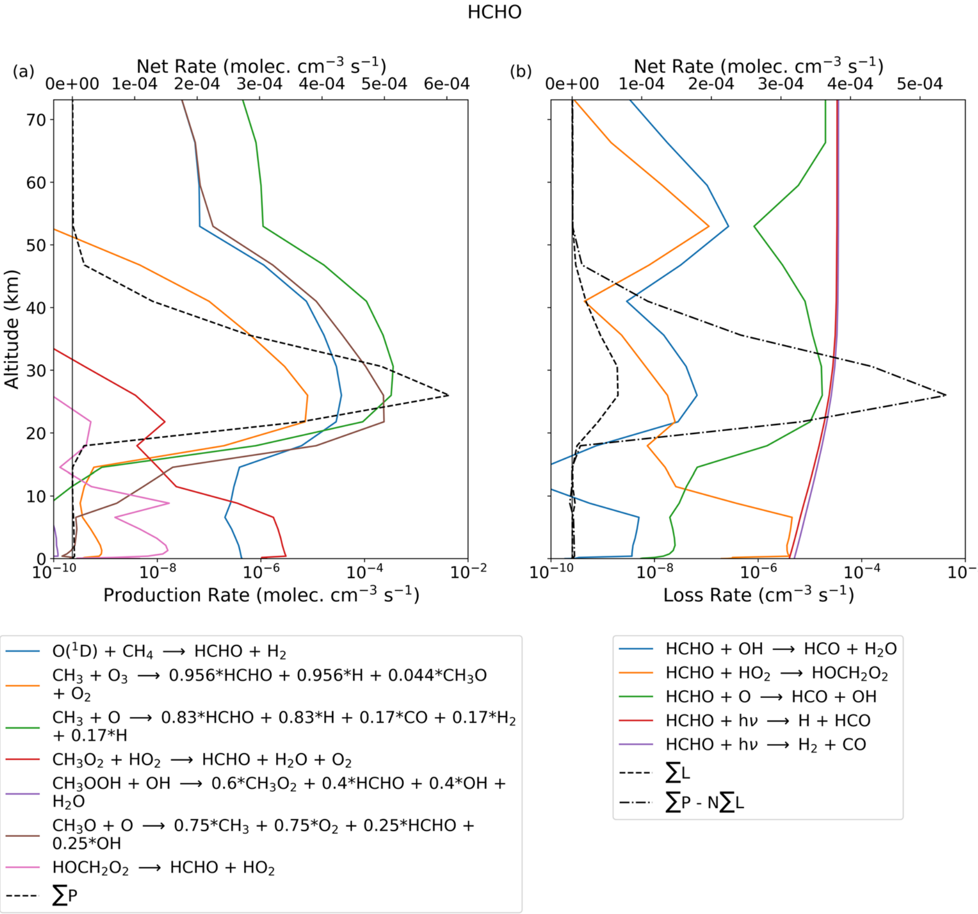

Figure 5. Photochemical production and loss rates for HCHO (molec $cm^{-3}s^{-1}$), associated with CH_4 photochemistry, as a function of altitude. Calculations are for L_S = 71°, 06:30 LT, and latitude 2.5° N.

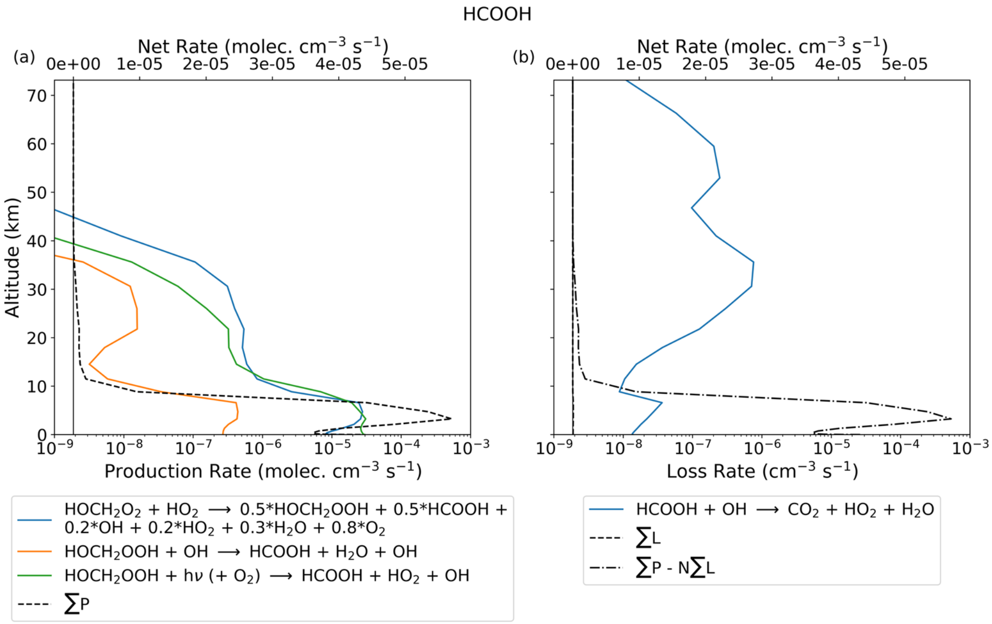

Figure 6. As Figure 5 but for formic acid (HCOOH).

3.2. Production of Formaldehyde from CH_4 Oxidation

HCHO is a high-yield oxidation product of CH_4 on Mars that is observable by the NOMAD and ACS spectrometers aboard the Trace Gas Orbiter. Figure 4 shows vertical distributions of HCHO volume mixing ratios, corresponding to a fixed vertical profile of 50 pptv CH_4, at 18:00 LT over all solar longitudes to determine when we might expect HCHO to be observable during one Martian year. HCHO production peaks during spring months when there is sufficient production of $O(^1D)$ in the middle atmosphere to oxidize CH_4 but not water vapor in the lower atmosphere. We find only small variations in the HCHO produced across the three latitudes, where HCHO consistently remains below 10^{-3} pptv. This lies well below the expected detection limit of 30–40 pptv for the TGO NOMAD instrument (Robert et al., 2016) and of 0.17–1.70 ppbv for the TGO ACS instrument (Korablev et al., 2017).

Figure 5 shows individual and net production and loss rates of HCHO as a function of altitude at 06:30 LT, $L_S = 71°$, and latitude 2.5° N. We find net production peaks at 06:30 LT as the Sun begins to rise above the horizon. Figure 5a shows two distinct regions where HCHO production peaks. Below the hygropause, at roughly 15 km at this L_S, reaction between water vapor and excited atomic oxygen result in HCHO production dominated by the reaction of CH_3O_2 and HO_2. Above the hygropause at 15 km, the HCHO production is from atomic oxygen reacting with methyl and methoxy radicals. Figure 5b show the HCHO loss rates. We find that HCHO is lost rapidly by photolysis through the atmospheric column. Below the hygropause, HCHO is lost by reaction with HO_2, which produced the $HOCH_2O_2$ peroxy radical. Above the hygropause, the dominant HCHO sink is reaction with atomic oxygen. At solar zenith angles between 60 and 85°, abundances of $O(^3P)$, CH_3, and CH_3O radicals are in large enough at the top of the hygropause to overcome the loss of HCHO from photolysis. At lower solar zenith angles, the rate of formaldehyde photolysis is too great to allow significant net production.

The resulting atmospheric lifetime of HCHO for all Martian seasons is 2–6 hours at latitudes less than 30° (Appendix A0.2), consistent with previously published results (Wong et al., 2003). As a result, a detection of HCHO below 70 km in the Martian atmosphere will require a strong active release of CH_4 in the local vicinity. Our calculations suggest that HCHO will be most likely detected at mid-altitudes (15–30 km) across the tropics during Mars northern spring and summer months. This is due to the lower abundance of water vapor and the increased levels of odd-oxygen species available for reactions with organic radicals and also coincides with the altitude regions where the TGO instruments are expected to display the greatest level of sensitivity (Korablev et al., 2017).

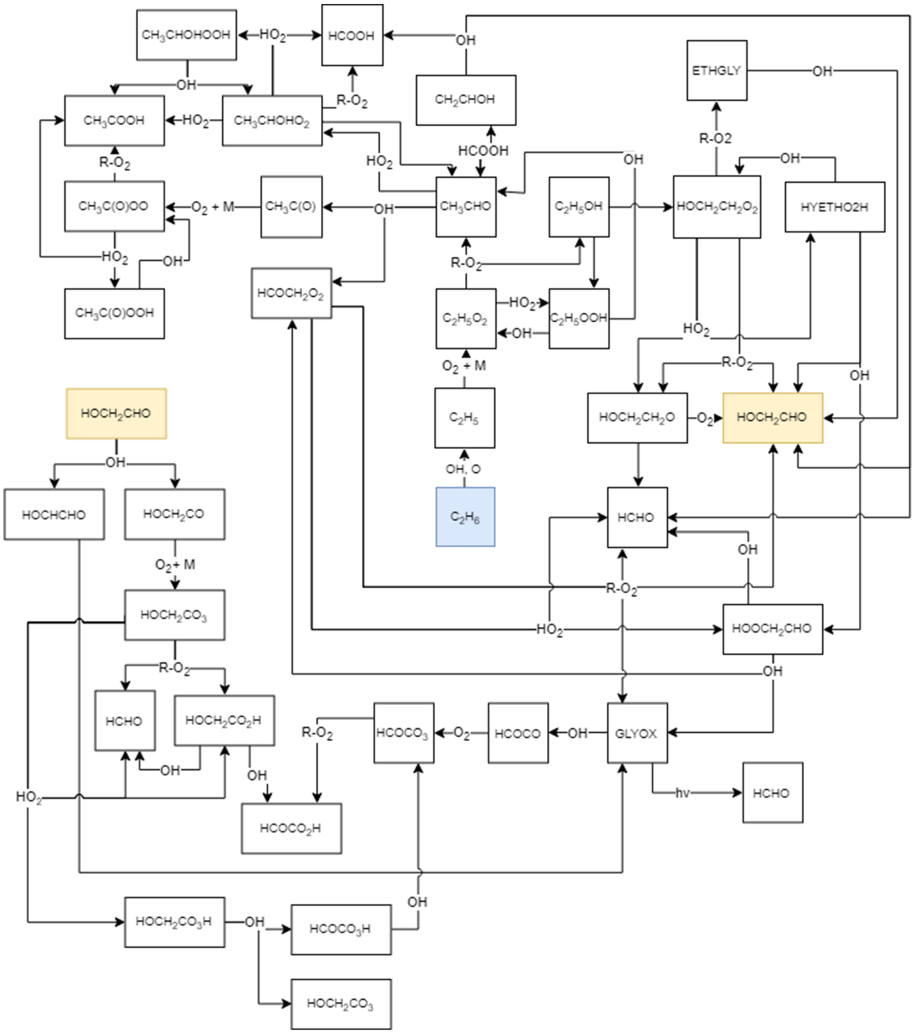

Figure 7. Primary stages of the C_2H_6 photochemistry that we use in out 1-D photochemistry submodule, taken from the CAABA/MECCA v4.0 box model.

Using 1-D steady-state model driven by a profile of 100 ppmv CH_4, (Wong et al., 2003) report an increase in HCHO above 50 km. Our 1-D calculations are time-dependent, driven by a more realistic CH_4 value (published since Wong et al., 2003) and by interpolated atmospheric parameters that include optical opacity and long-lived inorganic tracers from a 3-D data set. As such, we believe our approach provides a more comprehensive and realistic modeling environment to describe atmospheric photochemistry on Mars. The photolysis loss rates for HCHO in our model at latitude 2.5° are comparable to those used by (Wong et al., 2003). Differences between our calculations and those reported by (Wong et al., 2003) are mainly due to smaller quantities of radicals produced by a much lower assumed value of atmospheric CH_4 and our consideration of longitudinal mean variations of atmospheric parameters instead of using global mean parameters.

3.3. Production of Formic Acid from CH_4 Oxidation

The oxidation of HCHO via HO_2 radicals leads to pathways that produce HCOOH (Figure 1). HCHO reacts with HO_2 to produce the $HOCH_2O_2$ peroxy radical, which can either decay into its original reactants or react with HO_2 to produce HCOOH directly or to produce hydroxymethyl hydroperoxide that subsequently reacts with OH to produce formic acid or $HOCH_2O_2$, with a branching ratio, $k_{HOCH_2O_2}/k_{HCOOH}$, of 0.233 at 298 K. $HOCH_2OOH$ can also photolyse under UV radiation to produce $HOCH_2O$ and OH. The $HOCH_2O$ radical proceeds to react with molecular oxygen to produce formic acid and HO_2. The only sink of HCOOH in the Martian atmosphere is via oxidation by OH. This reaction is slow and limits loss of HCOOH to

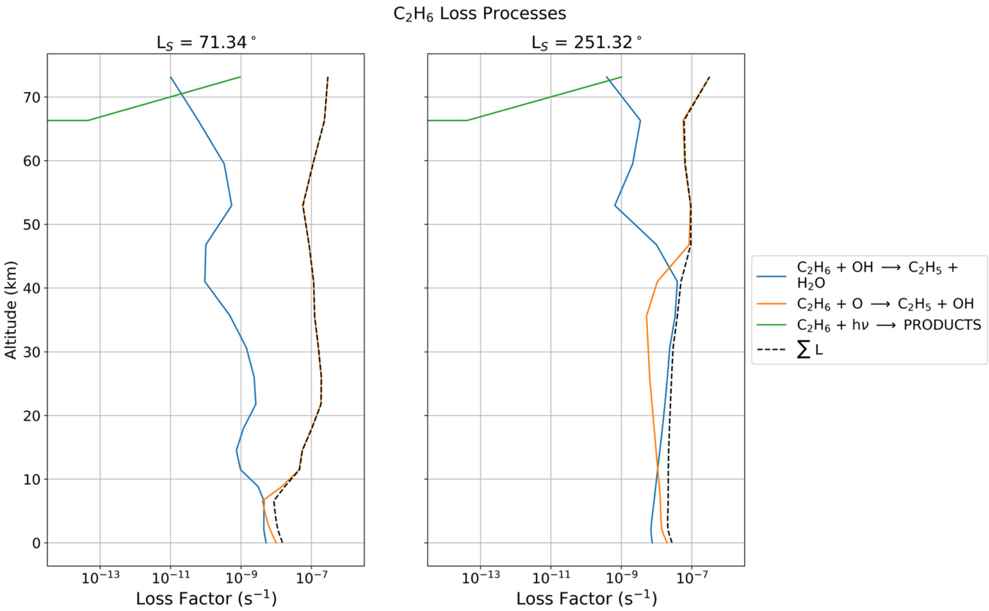

Figure 8. Photochemical loss factors for C_2H_6 as a function of altitude in our 1-D photochemistry model with altitude. Calculations are for L_S = 71° and 251°, 12:00 LT, at latitude 2.5° N.

regions below the point of the hygropause. In regions where OH concentrations are at a maximum, typically during L_S = 150–340° at the top of the water vapor saturation point, HCOOH has a photochemical lifetime that range between 1 and 10 sols. From the surface to roughly 8 km, values range between 70 and 220 sols throughout the year in the northern hemisphere, but values in the south increase to magnitudes of 10^3 sols during the northern summer (L_S = 90–180°) with the lower abundances of atmospheric H_2O.

Figure 6 shows the net and individual production and loss rates for HCOOH for L_S = 71°, latitude 2.5° N, and LT = 18:00 due to a fixed, uniformly distribution of 50 pptv CH_4. The largest production rate of HCOOH is from $HOCH_2O_2$ reacting with HO_2 and from the photolysis of $HOCH_2OOH$. The loss of HCOOH from OH oxidation is slow compared to the production rates. Our calculations therefore suggest that a detection of HCOOH would be related to the photochemical loss of HCHO. The resulting atmospheric lifetime of HCOOH is temporally and spatially variant, with lows of 2–5 sols at the tip of the hygropause, increasing to 75–100 sols closer to the surface where the abundances of OH fall.

3.4. Ethane Oxidation

Here, we consider the impact of C_2H_6 on Mars' photochemistry. The impetus for these calculations is that on Earth, emissions of CH_4 are accompanied by emissions of higher-chain hydrocarbon such as C_2H_6 (Guenther et al., 2000; Horita & Berndt, 1999). C_2H_6 is also listed as an observable compound through the NOMAD-SO and ACS-MIR instrument, with detection limits between 0.02 and 0.03 ppbv (Vandaele et al., 2018) and 0.06–6 ppbv (Korablev et al., 2017). Current knowledge puts an upper limit of 0.20 ppbv on C_2H_6 (Krasnopolsky, 2012; Villanueva et al., 2013).

Figure 7 shows that the photochemistry for C_2H_6 is more complicated than for CH_4 (B4) but follows the same general routes. It is oxidized by OH and $O(^1D)$ that initiates a series of chemical reactions that result in high yield products of HCHO and HCOOH among other compounds. One of the initial C_2H_6 oxidation product is the C_2H_5 radical, which is not described explicitly by the CAABA mechanism. We have used independent sources for reaction rates that involve the C_2H_5 radical (B5).

Figure 8 shows the photochemical loss factors for C_2H_6 in the Martian atmosphere at noon, L_S 71° and 251° and at latitude 2.5° N. Our photolysis calculations, based on values from the TUV model (Madronich et al., 2002) and adjusted for the Sun-Mars distance, suggest this loss process is insignificant below 70 km. Similar to CH_4, below the Martian hygropause OH is the dominant loss process for C_2H_6, and above the hygropause

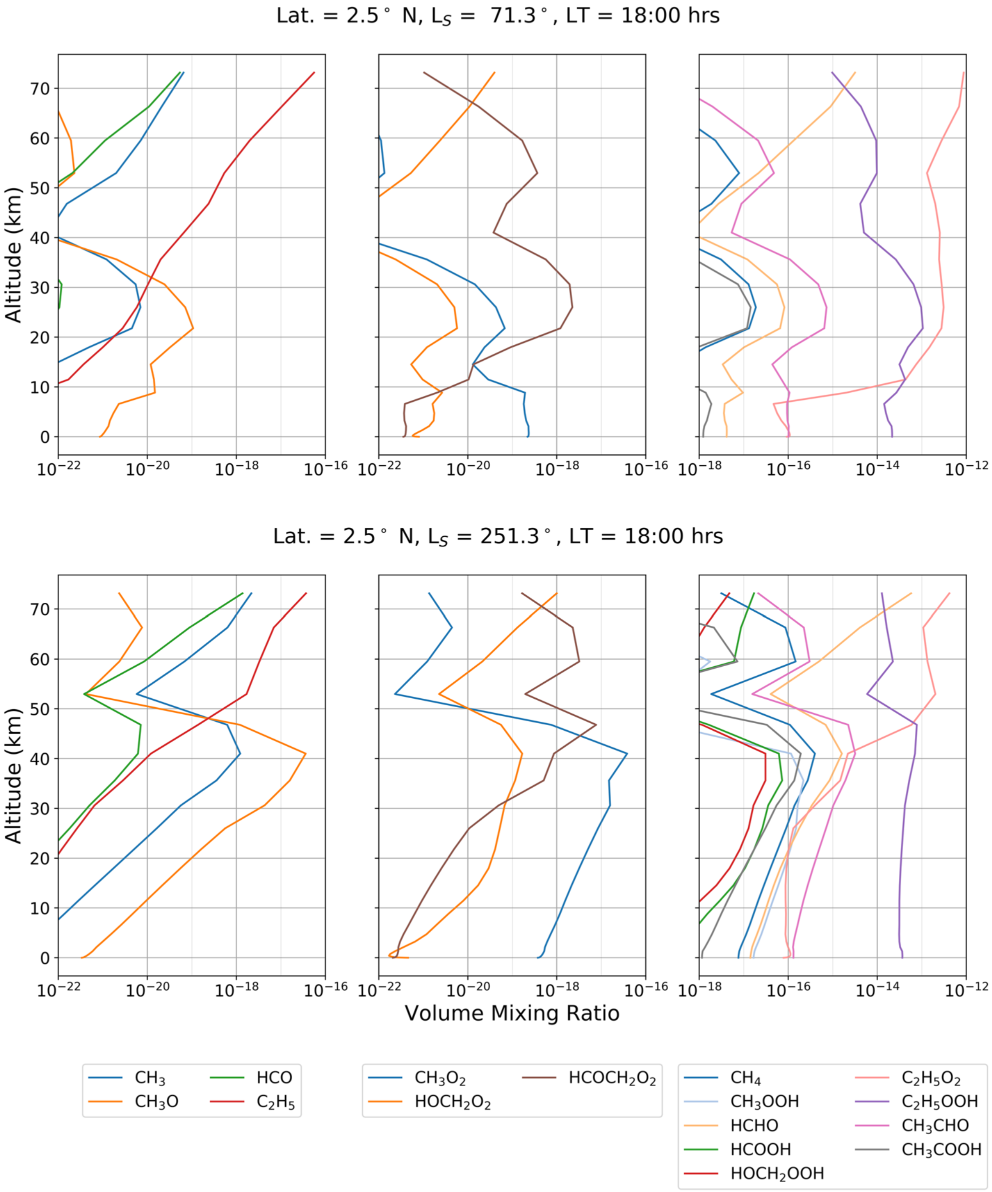

Figure 9. Volume mixing ratio profiles of oxidised organic products after one sol of introducing a uniform profile volume mixing ratio of 50 pptv of C_2H_6.

$O(^3P)$ is the dominant loss process for C_2H_6, with the $C_2H_5O_2$ peroxy radical being a common oxidation product that results in a cascade of photochemical reactions, as described in Figure 7. The resulting photochemical lifetime of C_2H_6 is typically between 1 and 3.5 years below altitudes of 5 km and much shorter (50–450 sols) above the hygropause. (A1).

Figure 9 shows the vertical profiles of organic compounds produced by the oxidation of 50 pptv of C_2H_6 after one sol at L_S 71° and 251°, latitude 2.5° sampled at 18:00 LT, to allow comparisons against the methane investigation of Figure 3. The introduction of longer chain peroxy-radicals via the $C_2H_5O_2$ radical increases the richness of photochemical products that are produced from CH_4 oxidation. In particular, the oxidation of C_2H_6 results in CH_3CHO column averaged mixing ratios of 7.24×10^{-16} molecule/molecule at aphelion conditions, elevating to 3.18×10^{-15} molecule/molecule at perihelion conditions. UV photolysis of CH_3CHO is a source of CH_4 and carbon monoxide. We find that UV photolysis of 50 pptv homogeneous column of C_2H_6 produces a CH_4 column averaged mixing ratio of 1.87×10^{-17} molecule/molecule at aphelion and 3.97×10^{-16} molecule/molecule at perihelion. The ratios of CH_4/C_2H_6 at aphelion and perihelion are 3.71×10^{-7} and

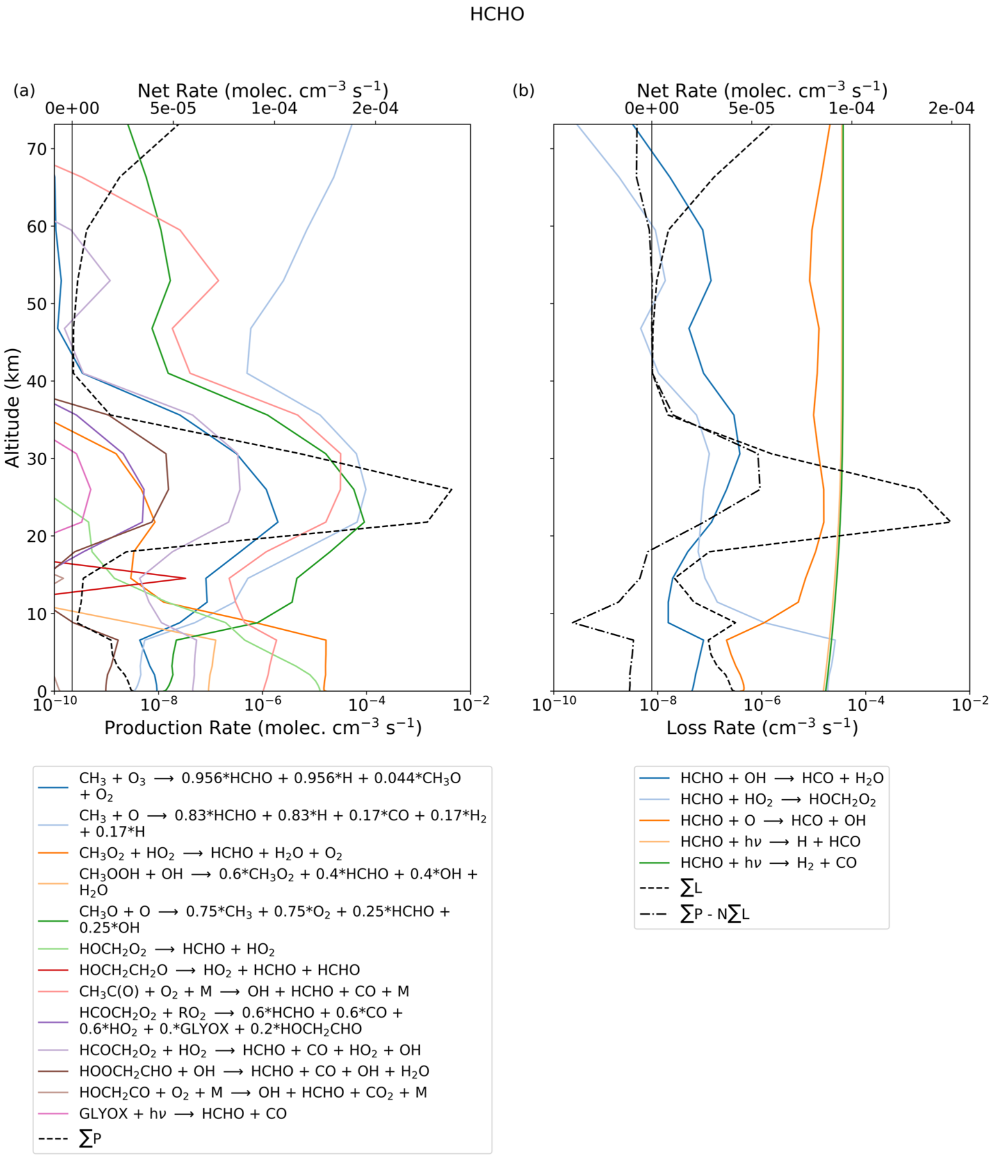

Figure 10. Photochemical production and loss rates (molec cm^{-3}s^{-1}) of HCHO and HCOOH in our 1-D photochemistry model associated with 50 pptv of C_2H_6. Values are for latitude 2.5° N, local time 12:00, and solar longitudes 71° and 251° as a function of altitude.

7.86×10^{-6}, respectively, and the ratio of CH_4/CH_3CHO at these two orbital points are 2.58×10^{-2} and 1.25×10^{-1}, respectively.

Formaldehyde is produced with a much higher yield for C_2H_6 oxidation than for CH_4 oxidation, resulting in a column averaged mixing ratio of 3.16×10^{-15} and 5.74×10^{-14} molecule/molecule at aphelion and perihelion, respectively. These yields are ≃6 times and 777 times higher than those made by CH_4 at aphelion and at perihelion, respectively. These higher yields of HCHO from C_2H_6 oxidation is due to a larger number of production pathways compared to the CH_4 oxidation mechanism. Production of HCOOH from C_2H_6 photochemistry during perihelion, column mixing ratio 7.30×10^{-17} molecule/molecule, is comparable with values from CH_4 oxidation but is much smaller than CH_4 oxidation during aphelion with a column mixing ratio of 1.34×10^{-18} molecule/molecule. Lower production of HCOOH from C_2H_6 oxidation during aphelion is due to lower production pathways for $HOCH_2OOH$ and $HOCH_2O_2$, which drive subsequent production of HCOOH.

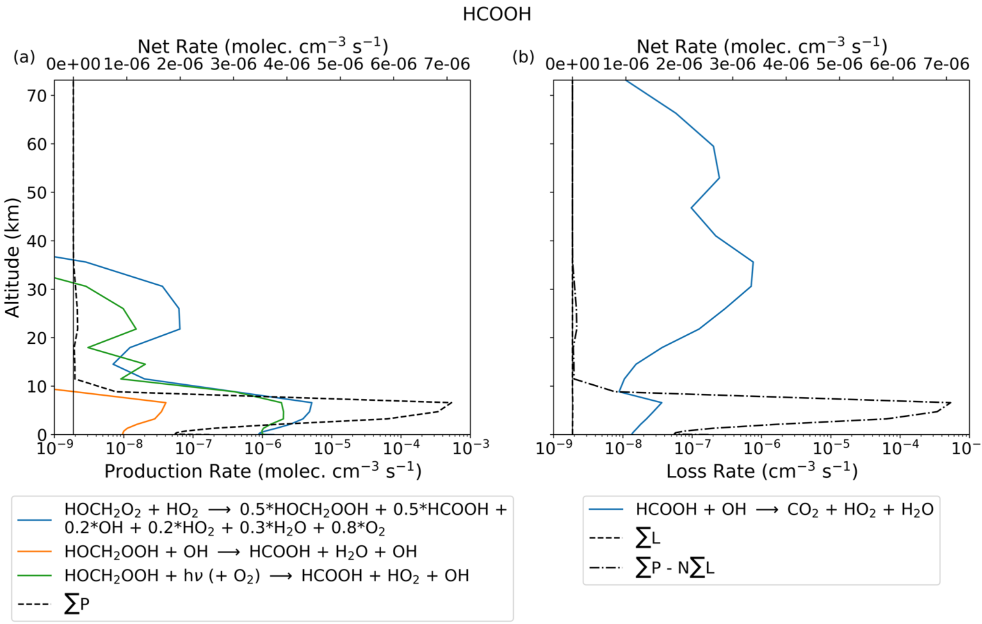

Figure 11. Photochemical production and loss rates for methane (molec cm^{-3}s^{-1}), associated with the UV photolysis of a 50 pptv column of CH_3CHO, as a function of altitude. Calculations are for $L_S = 251°$, 12:00 LT, and latitude 2.5° N.

3.5. Production of Formaldehyde and Formic Acid From C_2H_6 Oxidation

Figure 10 shows the production and loss rates for HCHO and HCOOH from the oxidation of 50 pptv of C_2H_6. The largest production rate of HCHO is below the hygropause from the reaction of CH_3O_2 peroxy radical with HO_2, comparable to values from CH_4 oxidation. However, above the hygropause at 20 km the three-body reaction $CH_3C(O)+O_2+M$ and the CH_3 radical reaction with atomic oxygen are the primary sources of HCHO. Combined, the HCHO production rate is an order of magnitude larger than the rate from CH_4 oxidation.

The higher reactivity of C_2H_6 produces a larger quantity of $HOCH_2O_2$ peroxy radicals and hydroperoxy radicals in the regions just above the hygropause compared to CH_4 oxidation. With no additional loss processes, the increased net production rate results in larger concentrations of HCOOH, with production falling off rapidly towards the surface.

3.6. Methane Production From the Oxidation of Acetaldehyde

Figure 11 shows production and loss rates of CH_4 associated with a 50 pptv homogeneous column of CH_3CHO at $L_S = 251°$, latitude 2.5°, and at local noon to study the importance of UV photolysis of CH_3CHO. We calculate the photolysis loss rate using the TUV model (section 2) that penetrate efficiently to the surface. Net CH_4 production rates peak at 31.13 molec cm^{-3} s^{-1}, corresponding to an increase in CH_4 mixing ratio of 1.69×10^{-16} molecule/molecule s^{-1}, at ≃1.30 km above the Martian surface at this time of day. To our knowledge, this photolytic source of atmospheric CH_4 is the only proposed source that may be possible within the CO_2-dominated atmosphere of Mars.

4. Discussion and Concluding Remarks

We find that the oxidation of atmospheric CH_4 in the Martian atmosphere, at magnitudes similar to reported observations, produces formaldehyde and formic acid as photochemical products but at volume mixing ratios too low for successful detection via remote sensing by the NOMAD and ACS spectrometers aboard the ExoMars Trace Gas Orbiter. Our photochemical lifetimes of formaldehyde are consistent with previous studies (e.g., Wong & Atreya, 2004), but we have also reported variations as a function of altitude and solar longitude. Our use of the MCD v5.3 atmospheric parameters and tracer profiles enabled us to deduce that the largest atmospheric lifetimes of HCHO at latitudes less than 30° are typically around 4 hours during the northern spring and summer above the point of H_2O vapor saturation. Our model expands upon the findings from the steady state model by revealing the layered seasonal structure of HCHO that can develop, while refining the modeled lifetimes and revealing the seasonal variability of the compound.

Our 1-D model refines the vertical structure and seasonal variability of the CH_4 within the equatorial regions of Mars, revealing that altitudes with low water vapor content can provide $O(^1D)$ abundances large enough to suppress the lifetime of CH_4 to between 50 and 100 years, shorter than previous estimates (Krasnopolsky et al., 2004; Summers et al., 2002; Wong & Atreya, 2004). We reveal a region in the upper section of the 1-D model, corresponding to 50–70 km, where the absence of OH, $O(^1D)$, and lower UV photolysis increases CH_4 lifetimes to 400–800 years during the northern spring and to 800–1,300 years during the mid-northern summer to northern winter, significantly higher than previous model estimations. Lifetimes close to the surface and below the hygropause (0–30 km) are invariant with latitude during the northern spring but display variations between the north and southern hemisphere throughout the rest of the year, controlled by the sublimation of the respective hemispheres polar caps water ice content.

We find that the photochemical lifetime of C_2H_6 is correlated to the atmospheric water vapor content on Mars. Within the hygropause, lifetimes are found to be within 3–4 years, where OH is the dominant photochemical sink. At higher altitudes, these lifetimes are reduced to 100–400 Mars sols (0.15–0.6 years), due to the higher abundance of atomic oxygen. The lifetimes of acetaldehyde reach values of approximately one sol close to the Martian surface across all equatorial latitudes during the northern spring that lower to roughly 0.5 sols in the northern hemisphere summer to winter periods. Acetic acid displays a similar seasonal trend, with lifetimes in the northern spring being between 3 and 4 sols below the hygropause, and lowering to between 0.2–1 sol with the elevation of the water saturation point. Oxidation of C_2H_6 in the Martian atmosphere results in a distinct profile of acetaldehyde, as well as greater yields of HCHO and HCOOH, compared to CH_4 oxidation. The 1-D model predicts atmospheric lifetimes of between 15 and 32 hours below altitudes of 25 km during $L_S = 0–135°$, lowering to 4–12 hours outside of this time frame across all equatorial latitudes, for CH_3CHO. We therefore propose that any instrument detection of CH_3CHO can be attributed to a surface release of C_2H_6 within the immediate local environment of the site of observation.

Our more comprehensive description of atmospheric chemistry, involving 135 organic reactions, significantly expands on the schemes used by Wong and Atreya (2004) and Summers et al. (2002). No formic acid was reported by the model of Wong and Atreya (2004) for their 1-D steady state model with 100 ppmv of CH_4, whereas we report volume mixing ratios of similar magnitude to HCHO below the hygropause with CH_4 abundances of 50 pptv, the current upper limit on Mars derived in Korablev et al. (2019). This discrepancy can be explained by our more detailed description of peroxy radical chemistry that is taken from the CAABA/MECCA v4.0 chemistry scheme. In our 1-D model, photochemical lifetimes of HCOOH are inversely proportional to the abundance of OH available. At the top of the hygropause, lifetimes have magnitudes of 1–10 sols. Below, the lifetimes vary substantially depending on the water vapor availability. Below 5 km, photochemical lifetimes in the drier southern latitudes can reach values exceeding 10^3 sols, whereas in the north, values between 10 and 100 are commonly found. These long photochemical lifetimes of HCOOH, in comparison to HCHO, make it the most likely photochemical product of CH_4 oxidation that could provide independent verification of CH_4. Spectral features of HCOOH lie within the IR wavelengths measured by the ACS aboard the TGO, and the long wave channel of the PFS covers the wavenumber range of 250–1,700 cm^{-1} (Formisano et al., 2005) that includes two absorption features of the HCOOH molecule (Gordon et al., 2017).

We find that the introduction of CH_4 at magnitudes similar to an empirically derived upper limit (<50 pptv) fails to produce significant perturbations to CO, O_3, or H_2O vapor (not shown) that will observable by instruments aboard the TGO. CH_4 reactions with $O(^1D)$ above the hygropause and below 50 km have the net effect of increasing OH concentrations by magnitudes of 10^{-3}% after one sol of exposure, which results in catalyzing the conversion of CO to CO_2 via reaction e_1 of B1. The increase in OH arises from the previously described reactions of $O(^1D)$ atoms reacting with CH_4 in the drier altitudes, most notably reaction b_7. CO experiences relative perturbations of -10^{-6}% in the mid-altitudes, which will be lost within instrumental noise. This rise in OH, and the loss of $O(^1D)$ to CH_4 interactions and $O(^3P)$ with organic radical interactions, results in a drop in O_3 production in this region and increased O_3 loss. These perturbations are small, however, with drops of 10^{-3}% after one sol, an amount that is below instrument signal-to-noise values. This

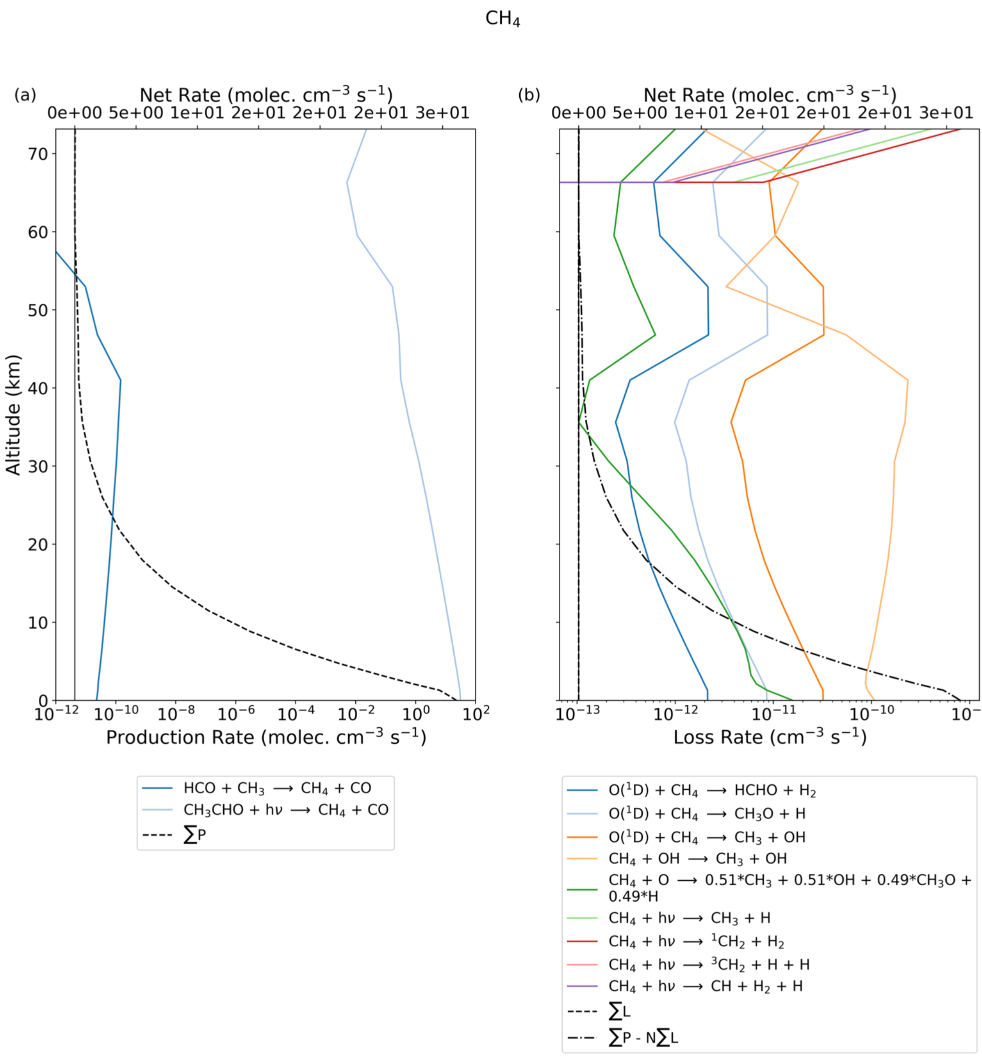

Figure A1. Local and vertically integrated photochemical lifetime of CH_4 within the atmosphere of Mars and its variations with altitude (km) and solar longitude at latitudes 30° N, 2.5° N, and 30° S, respectively. All vertical segments are values from the 1-D photochemistry model at 12:00 LT.

highlights that source regions of CH_4 will not be identifiable by perturbations made to inorganic trace gas species observable to the ExoMars Trace Gas Orbiter.

Finally, our model highlights the possible existence of an atmospheric source of CH_4 from the photolysis of CH_3CHO, an oxidation product of C_2H_6. Photolysis of CH_3CHO in the Martian atmosphere is capable of producing trace amounts of CH_4 at all altitudes above the surface. We find that 50 pptv of CH_3CHO is capable of producing CH_4 at a volume mixing ratio rate of 4.54×10^{-16} s^{-1}.

This opens up the possibility of further studying CH_3CHO as a possible source for CH_4 detection on Mars. Although no evidence exists for CH_3CHO on Mars, one hypothetical source could be due to a subsurface acetylene hydratase (Rosner & Schink, 1995) enzyme that converts acetylene (C_2H_2) to CH_3CHO through reactions with liquid water.

Appendix A: Martian Atmospheric Lifetimes of Methane, Formaldehyde, Formic Acid, and Ethane

A1 Methane

Figure A1 shows the net atmospheric lifetime of CH_4, incorporating all loss terms (Figure 2), as a function of latitude and solar longitude. Atmospheric lifetimes reach a minimum of 25–400 years between the top of the

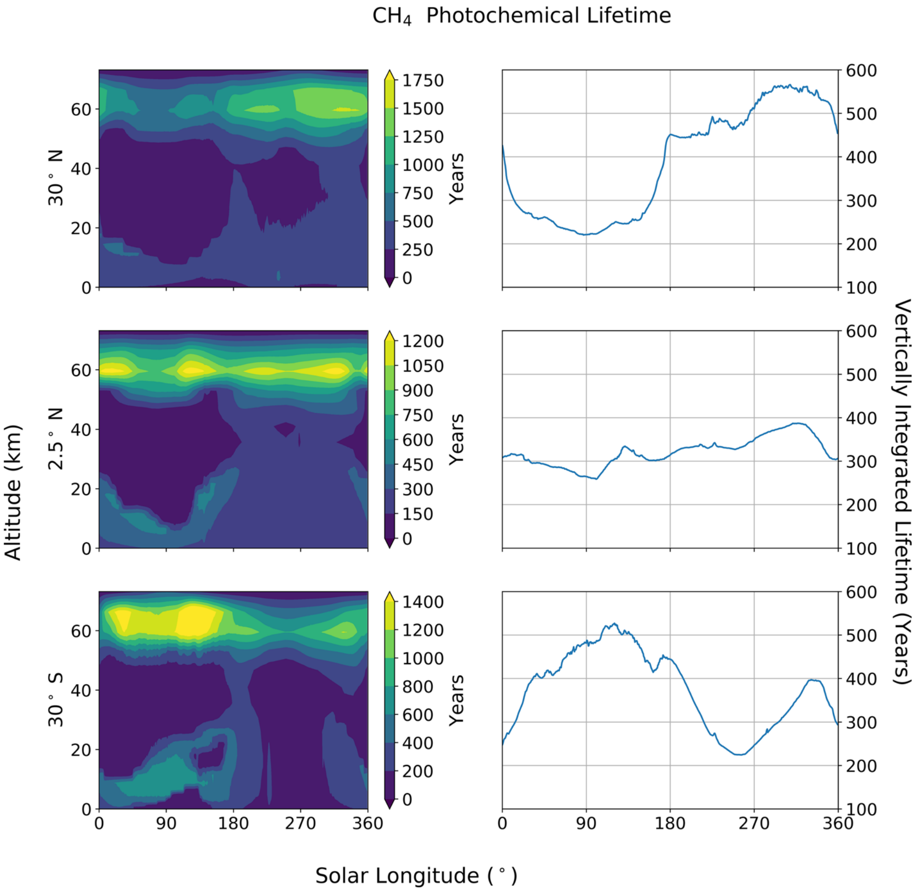

Figure A2. Photochemical lifetime of HCHO within the atmosphere of Mars and its variations with altitude (km) and solar longitude at latitudes 30° N, 2.5° N, and 30° S, respectively. All vertical segments are values from the 1-D photochemistry model at 12:00 LT.

hygropause and approximately 50 km due to the larger abundance of the O(^{1}D) atom. Below the hygropause where OH is the dominant sink, atmospheric lifetimes vary between 400 and 800 years. The longest lifetimes of 800–1,600 years lie between 50 and 60 km during winter (L_S = 270–360°), as described above, where the OH and O(^{1}D) loss processes decline and before photolysis dominates above 60 km.

Variations in atmospheric lifetime are driven by the position of the Martian hygropause and the water vapor content beneath, which is determined by 3-D model output from the MCD (section 2). Water vapor columns reach their maximum during hemispheric summer months when polar water ice sublimates with rising atmospheric temperatures. SPICAM water vapor column measurements at L_S = 50° (Fedorova et al., 2006) show only small variations at latitudes less than 30°, with values ranging from 2–10 pr μm, with saturation values under 25 km. This is consistent with our model loss processes that determine the variation in atmospheric lifetime. Above 50 km, the stronger flux of solar radiation in the northern hemisphere due to the planets axial tilt results in a larger abundance of O(^{1}D) and a subsequent lower photochemical lifetime of CH_4 than in the southern hemisphere. As water vapor column abundances and saturation

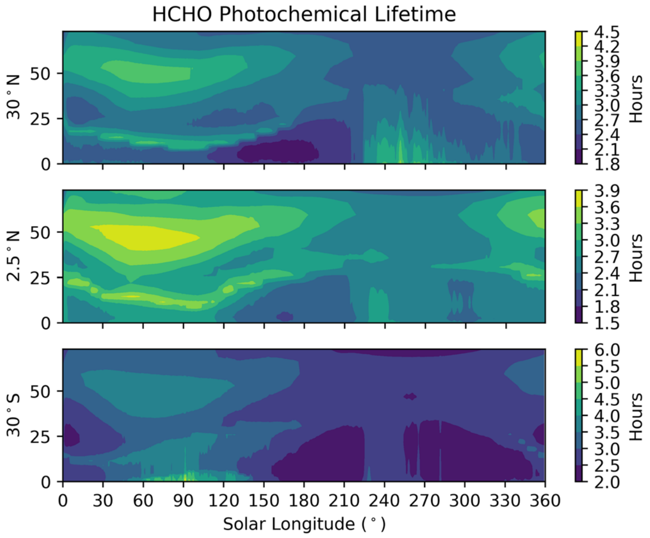

Figure A3. Photochemical lifetime of HCOOH within the atmosphere of Mars and its variations with altitude (km) and solar longitude at latitudes 30° N, 2.5° N, and 30° S, respectively. All vertical segments are values from the 1-D photochemistry model at 12:00 LT. Contour map saturated for values greater than 0.45 years.

altitudes increase with L_S, the low latitude atmospheric lifetime of CH_4 increases below 50 km due to H_2O reacting with $O(^1D)$ and decreases below roughly 25 km. The decrease in solar flux during northern autumn and winter months ($L_S = 180°–360°$) reduces the production rate of $O(^1D)$ relative to the southern hemisphere, which explains the variation in lifetimes between the hemispheres.

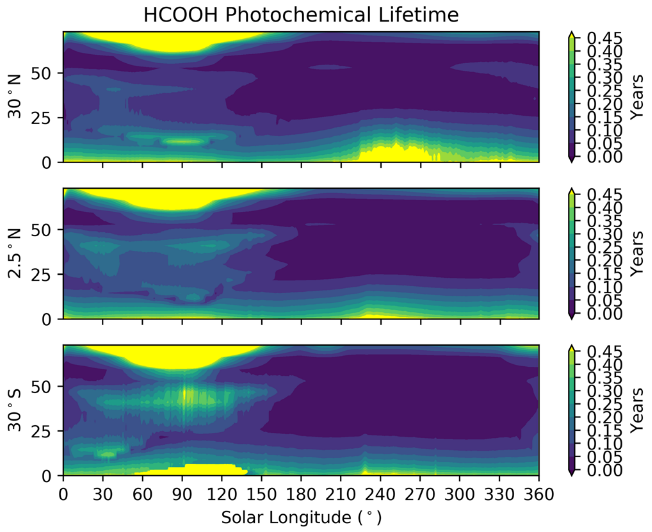

Figure A4. Local and vertically integrated photochemical lifetime of C_2H_6 within the atmosphere of Mars and its variations with altitude (km) and solar longitude at latitudes 30° N, 2.5 ° N, and 30° S, respectively. All vertical segments are values from the 1-D photochemistry model at 12:00 LT.

A2 Formaldehyde

Figure A2 shows the resultant seasonal variability of HCHO lifetime at latitudes 30° N, 2.5° N, and 30° S. We find the longest lifetimes, between 4 and 5 hours, are found below 5 km in the southern hemisphere during the northern summer/southern winter, when this region contains low levels of water vapor.

A3 Formic Acid

Figure A3 shows the resultant seasonal variability of HCOOH lifetime at latitudes 30° N, 2.5° N, and 30° S. The lifetime of HCOOH is anticorrelated with water vapor, as expected. The longest lifetime (of magnitude's greater than 10^4 sols) is during the northern spring at altitudes greater than 60 km where OH is lowest. As OH values increase with the supply of water vapor from northern polar ice sublimation, atmospheric lifetimes falls to 1–10 sols close to the hygropause and 10–200 sols at lower altitudes closer to the surface (below 5 km).

With atmospheric lifetimes of this length, describing seasonal changes in HCOOH profiles using a 1-D photochemistry model becomes problematic due to the photochemical lifetimes exceeding the venting timescales associated with our 3.75° thick zonal band that our model represents. Without horizontal transport equations to describe the loss of HCOOH to the zonal band edges, the resultant profiles after a one-year 1-D model run will be subject to gross inaccuracies. As previously discussed in section 2, solving the 1-D model equation for steady state conditions will not yield useful information due to the observed temporal and localized nature of CH_4 emissions, invalidating the notion of a steady-state environment.

A4 Ethane

Figure A4 shows that C_2H_6 has longer photochemical lifetimes below the points of H_2O saturation, where we find typical values that range from 3 to 5 years. In the middle atmosphere, the large abundance of $O(^3P)$ reduced the lifetime to 30–450 sols. Based on these calculations, we suggest that any detection of C_2H_6 made by the TGO instruments will due to an active release.

Appendix B: Reaction Rate Coefficients

Data Availability Statement

The 1-D photochemistry model code used to construct this work has been frozen and stored on Zenodo, (Taysum, 2020a). The data sets containing the atmospheric parameters and tracer mixing ratio profiles constructed from the Mars Climate Database v5.3 are also stored on Zenodo, (Taysum, 2020b). All output files produced by the 1-D model used in this work and plotting routines used to construct the figures and extract numerical data from the files are stored on Zenodo, (Taysum, 2020). The TUV model source code used to construct the J-value look-up tables can be acquired through the url (https://www2.acom.ucar.edu/modeling/tropospheric-ultraviolet-and-visible-tuv-radiation-model). The Mars Climate Database v5.3 source code used to create the offline tables for atmospheric parameter and long-lived tracer vmr's for the 1-D model here can be acquired through the url (http://www-mars.lmd.jussieu.fr/mars/access.html), requiring a request to be made to the researchers listed on the site.

Table B1

Inorganic Reaction Rate Coefficients Within the 1-D Photochemistry Submodule

Key	Reaction	Formula	Rate at T = 298 K	Reference
Reactions with O				
a_1	$O+O_2+M \rightarrow O_3+M$	2.075 × 6.00E-34(T/300)$^{-2.4}$	2.23E-16 ^{a}	(Sander et al., 2003)
a_2	$O+O+M \rightarrow O_2+M$	2.50 × 9.46E-34exp(485/T)	2.10E-15 ^{a}	(Campbell & Gray, 1973)
a_3	$O+O_3 \rightarrow O_2+O_2$	8.00E-13exp(-2060/T)	7.96E-16	(Sander et al., 2003)
Reactions with O(^{1}D)				
b_1	$O(^1D)+CO_2 \rightarrow O+CO_2$	7.40E-11exp(120/T)	1.11E-10	(Sander et al., 2003)
b_2	$O(^1D)+H_2O \rightarrow OH+OH$	1.63E-10exp(60/T)	1.99E-10	(Sander et al., 2006)
b_3	$O(^1D)+H_2 \rightarrow OH+H$	1.20E-10	1.20E-10	(Sander et al., 2011)
b_4	$O(^1D)+O_2 \rightarrow O+O_2$	3.30E-11exp(55/T)	3.97E-11	(Sander et al., 2006)
b_5	$O(^1D)+O_3 \rightarrow O_2+O_2$	1.20E-11	1.20E-11	(Sander et al., 2003)
b_6	$O(^1D)+O_3 \rightarrow O_2+O+O$	1.20E-11	1.20E-11	(Sander et al., 2003)
b_7	$O(^1D)+CH_4 \rightarrow CH_3+OH$	0.75 × 1.75E-10	1.31E-10	(Sander et al., 2003)
b_8	$O(^1D)+CH_4 \rightarrow CH_3O+H$	0.20 × 1.75E-10	3.50E-11	(Sander et al., 2003)
b_9	$O(^1D)+CH_4 \rightarrow HCHO+H_2$	0.05 × 1.75E-10	8.75E-12	(Sander et al., 2003)
Reactions with Hydrogen Compounds				
c_1	$O+HO_2 \rightarrow OH+O_2$	3.00E-11exp(200/T)	5.87E-11	(Sander et al., 2003)
c_2	$O+OH \rightarrow O_2+H$	1.80E-11exp(180/T)	3.29E-11	(Sander et al., 2011)
c_3	$H+O_3 \rightarrow OH+O_2$	1.40E-10exp(-470/T)	2.89E-11	(Sander et al., 2003)
c_4	$H+HO_2 \rightarrow OH+OH$	7.20E-11	7.20E-11	(Sander et al., 2006)
c_5	$H+HO_2 \rightarrow H_2+O_2$	6.90E-12	6.90E-12	(Sander et al., 2006)
c_6	$H+HO_2 \rightarrow H_2O+O$	1.60E-12	1.60E-12	(Sander et al., 2006)
c_7	$OH+HO_2 \rightarrow H_2O+O_2$	4.80E-11exp(250/T)	1.11E-10	(Sander et al., 2003)
c_8	$HO_2+HO_2 \rightarrow H_2O_2+O_2$	1.50E-12exp(19/T)	1.60E-12	(Christensen et al., 2002)
c_9	$OH+H_2O_2 \rightarrow H_2O+HO_2$	1.80E-12	1.80E-12	(Sander et al., 2006)
c_{10}	$OH+H_2 \rightarrow H_2O+H$	2.80E-12exp(-1800/T)	6.67E-15	(Sander et al., 2006)
c_{11}	$H+O_2+M \rightarrow HO_2+M$	k_3rd(2.5 × 4.4E-32, -1.3, 7.5E-11, 0.2)	1.88E-14 ^{a}	(Sander et al., 2011)
c_{12}	$O+H_2O_2 \rightarrow OH+HO_2$	1.40E-12exp(-2000/T)	1.70E-15	(Sander et al., 2003)
c_{13}	$OH+OH \rightarrow H_2O+O$	1.80E-12	1.80E-12	(Sander et al., 2006)
c_{14}	$OH+O_3 \rightarrow HO_2+O_2$	1.50E-12exp(-880/T)	7.83E-14	(Sander et al., 2003)
c_{15}	$HO_2+O_3 \rightarrow OH+O_2+O_2$	1.00E-14exp(-490/T)	1.93E-15	(Sander et al., 2003)
c_{16}	$HO_2+HO_2+M \rightarrow H_2O_2+O_2+M$	2.50 × 2.10E-33exp(920/T)	2.01E-14 ^{a}	(Sander et al., 2011)
c_{17}	$OH+OH+M \rightarrow H_2O_2+M$	k_3rd(2.5 × 6.9E-31, -1, 2.60E-11, 0)	2.70E-13 ^{a}	(Sander et al., 2003)
c_{18}	$H+H+M \rightarrow H_2+M$	2.5 × 1.80E-30/T	2.64E-14 ^{a}	(Baulch et al., 2005)
Carbon Compounds				
e_1	$OH+CO \rightarrow CO_2+H$	Details in Joshi and Wang (2006)	1.47E-13	(Joshi & Wang, 2006)
e_2	$O+CO+M \rightarrow CO_2+M$	2.5 × 6.50E-33exp(-2184/T)	1.87E-18 ^{a}	(Tsang & Hampson, 1986)

Note. Bimolecular rate coefficient units are cm^3 molec^{-1} s^{-1}. Values denoted by superscript *a* are three-body reactions with values taken with atmospheric number density complying to temperatures of T = 298 K and pressures of 660 Pa.

Table B2
Photolytic Reactions of Inorganic Compounds Used Within the 1-D Photochemistry Submodule

Key	Reaction	J(z = 0.50 km)	J(z = 42.67 km)
$j_{O_2 \rightarrow O)}$	$O_2+h\nu \rightarrow O+O$	2.95E-10	5.16E-09
$j_{O_2 \rightarrow O(^1D)}$	$O_2+h\nu \rightarrow O+O(^1D)$	0	0
$j_{CO_2 \rightarrow O}$	$CO_2+h\nu \rightarrow CO+O$	3.79E-12	1.02E-10
$j_{CO_2 \rightarrow O(^1D)}$	$CO_2+h\nu \rightarrow CO+O(^1D)$	0	0
$j_{O_3 \rightarrow O(^1D)}$	$O_3+h\nu \rightarrow O_2+O(^1D)$	3.12E-03	4.09E-03
$j_{O_3 \rightarrow O}$	$O_3+h\nu \rightarrow O_2+O$	5.22E-04	6.86E-04
j_{H_2O}	$H_2O+h\nu \rightarrow H+OH$	1.28E-10	4.67E-08
$j_{H_2O_2}$	$H_2O_2+h\nu \rightarrow OH+OH$	3.93E-05	5.26E-05
j_{HO_2}	$HO_2+h\nu \rightarrow O+OH$	2.40E-04	3.20E-04

Note. Values (s^{-1}) are interpolated from an offline look-up table constructed by a modified TUV (Madronich et al., 2002) model with respect to CO_2 and O_3 column abundances overheard, temperature, optical opacity, and solar zenith angle. Values displayed are for a solar zenith angle of 0°, $L_S = 251°$ (perihelion).

Table B3
Functions and Constants Used by the R-O_2 Permutation Reaction Handling Scheme Extracted From the CAABA/MECCA v4.0 Box Model

CAABA/MECCA v4.0 reaction rate parameters		
Key	Formula	Notes and citations
Radical Arrhenius equations		
k_ch3o2	1.03E-13*exp(365/T)	CH_3O_2 Self-reaction (Sander et al., 2019)
k_ch3ooh	5.30E-12*exp(190/T)	CH_3OOH + OH Reaction (Sander et al., 2019)
k_ch3co2h	4.00E-14*exp(850/T)	CH_3CO_2H + OH Reaction (Sander et al., 2019)
k_ro2ho2_1	2.91E-13*exp(1300/T)*(1 - exp(-0.245*1))	RO_2+HO_2 (One carbon atom) (Sander et al., 2019)
k_ro2ho2_2	2.91E-13*exp(1300/T)*(1 - exp(-0.245*2))	RO_2+HO_2 (Two carbon atoms) (Sander et al., 2019)
Arrhenius equations for H abstraction by OH		
k_s	4.50E-18*T^2*exp(253./T)	(Taraborrelli, 2010; Sander et al., 2019)
k_t	2.12E-18*T^2*exp(696/T)	(Taraborrelli, 2010; Sander et al., 2019)
k_rohro	2.10E-18*T^2*exp(-85/T)	(Taraborrelli, 2010; Sander et al., 2019)
k_roohro	0.60*k_ch3ooh	(Taraborrelli, 2010; Sander et al., 2019)
k_co2h	0.7*k_ch3co2h	(Taraborrelli, 2010; Sander et al., 2019)
kdec	1.00E6	(Atkinson et al., 2006; Sander et al., 2019)
Updated rate constants for RO_3+HO_2 reactions		
kapho2	5.20E-13*exp(980/T)*1.865	(Groß et al., 2014; Sander et al., 2019)
Arrhenius equations for permutation reactions		
k_ro2soro2	2*(7.70E-15*exp(1330/T)*k_ch3o2)$^{0.5}$	(Sander et al., 2019)
k_ro2rco3	4.00E-12*exp(500/T)	(Sander et al., 2019)
k_ro2poro2	2*7.50E-14*exp(500/T)	(Sander et al., 2019)
Substituent factors		
f_soh	3.44	(Taraborrelli, 2010; Sander et al., 2019)
f_sooh	8.00	(Taraborrelli, 2010; Sander et al., 2019)
f_pch2oh	1.29	(Taraborrelli, 2010; Sander et al., 2019)
f_tooh	8.00	(Taraborrelli, 2010; Sander et al., 2019)
f_toh	2.68	(Taraborrelli, 2010; Sander et al., 2019)
f_o	8.15	(Taraborrelli, 2010; Sander et al., 2019)
f_cho	0.55	(Taraborrelli, 2010; Sander et al., 2019)
f_co2h	1.67	(Taraborrelli, 2010; Sander et al., 2019)
Branching ratios for RO_2+HO_2 reactions		
rco3_o3	0.10	(Groß et al., 2014; Sander et al., 2019)
rco3_oh	0.69	(Groß et al., 2014; Sander et al., 2019)
rco3_ooh	0.21	(Groß et al., 2014; Sander et al., 2019)

Table B3
Continued

CAABA/MECCA v4.0 reaction rate parameters		
rchoch2o2_oh	0.10	(Sander et al., 2019)
rcoch2o2_oh	0.15	(Sander et al., 2019)
rcoch2o2_ooh	0.85	(Sander et al., 2019)

Table B4
Chemical Reactions and Rate Coefficients Involved in the Oxidation of CH_4 Used in Our 1-D Photochemistry Model

Methane reaction scheme

Key	Reaction	Formula	Rate at T = 298 K	Reference
cab_1	$CH_4+OH \rightarrow CH_3+OH$	1.85E-20exp(2.82LOG(T) - 987./T)	6.40E-15	(Sander et al., 2019)
cab_2	$CH_4+O \rightarrow 0.51{\ast}CH_3+0.51{\ast}OH$ $+0.49{\ast}CH_3O+0.49{\ast}H$	6.03E-18($T^{2.17}$)exp(-3619/T)	7.50E-18	(Sander et al., 2019)
cab_3	$CH_3+O_2+M \rightarrow CH_3O_2+M$	k_3rd(7.00E-31, 3., 1.80E-12, -1.1)	1.14E-13 [a]	(Sander et al., 2019)
cab_4	$CH_3+O_3 \rightarrow 0.956{\ast}HCHO+0.956{\ast}H$ $+0.044{\ast}CH_3O+O_2$	5.10E-12exp(-210/T)	2.52E-12	(Sander et al., 2019)
cab_5	$CH_3+O \rightarrow 0.83{\ast}HCHO+0.83{\ast}H$ $+0.17{\ast}CO+0.17{\ast}H_2+0.17{\ast}H$	1.30E-10	1.3E-10	(Sander et al., 2019)
cab_6	$CH_3O_2+HO_2 \rightarrow CH_3OOH+O_2$	3.8E-13exp(780/T) /(1 + 1/(498exp(1160/T)))	5.21E-12	(Sander et al., 2019)
cab_7	$CH_3O_2+HO_2 \rightarrow HCHO+H_2O+O_2$	3.8E-13exp(780/T) /(1 + 498exp(-1,160/T)))	4.67E-13	(Sander et al., 2019)
cab_8	$CH_3O_2+R-O_2 \rightarrow CH_3O+0.5{\ast}O_2$	2 × 7.40E-13exp(-520/T)	2.59E-13	(Sander et al., 2019)
cab_9	$CH_3O_2+R-O_2 \rightarrow 0.5{\ast}HCHO$ $+0.5{\ast}CH_3OH+0.5{\ast}O_2$	2 × (k_ch3o2 - 7.40E-13exp(-520/T))	4.43E-13	(Sander et al., 2019)
cab_{10}	$CH_3O_2+O_3 \rightarrow CH_3O+O_2+O_2$	2.90E-16exp(-1,000/T)	1.01E-17	(Sander et al., 2019)
cab_{11}	$CH_3O_2+OH \rightarrow CH_3O+HO_2$	1.40E-10	1.40E-10	(Sander et al., 2019)
cab_{12}	$CH_3O_2+O \rightarrow CH_3O+O_2$	4.30E-11	4.30E-11	(Sander et al., 2019)
cab_{13}	$CH_3OH+OH \rightarrow 0.85{\ast}HCHO$ $+0.85{\ast}HO_2+0.15{\ast}CH_3O+H_2O$	6.38E-18(T^2)exp(144/T)	9.19E-13	(Sander et al., 2019)
cab_{14}	$CH_3OOH+OH \rightarrow 0.6{\ast}CH_3O_2$ $+0.4{\ast}HCHO+0.4{\ast}OH+H_2O$	k_ch3ooh_oh	1.00E-11	(Sander et al., 2019)
cab_{15}	$CH_3O+O_2 \rightarrow HO_2+HCHO$	1.30E-14exp(-633/T)	1.55E-15	(Sander et al., 2019)
cab_{16}	$CH_3O+O_3 \rightarrow CH_3O_2+O_2$	2.53E-14	2.53E-14	(Sander et al., 2019)
cab_{17}	$CH_3O+O \rightarrow 0.75{\ast}CH_3+0.75{\ast}O_2$ $+0.25{\ast}HCHO+0.25{\ast}OH$	2.50e-11	2.50E-11	(Sander et al., 2019)
cab_{18}	$HCHO+OH \rightarrow HCO+H_2O$	5.50E-12exp(-125/T)	3.60e-12	(Sander et al., 2011)
cab_{19}	$HCHO+HO_2 \rightarrow HOCH_2O_2$	9.70E-15exp(625/T)	7.90E-14	(Sander et al., 2019)
cab_{20}	$HCHO+O \rightarrow HCO+OH$	2.99E-11exp(-1,529/T)	1.77E-13	(Herron, 1988)
cab_{21}	$HCO+O \rightarrow CO+OH$	5.00E-11	5.00E-11	(Baulch et al., 1992)
cab_{22}	$HCO+CH_3 \rightarrow CH_4+CO$	4.40E-11	4.40E-11	(Mulenko, 1987)
cab_{23}	$HCO+CH_3 \rightarrow CH_3CHO$	4.42E-11	4.42E-11	(Mulenko, 1980)
cab_{24}	$HCO+HCO \rightarrow HCHO+CO$	4.48E-11	4.48E-11	(Friedrichs et al., 2002)
cab_{25}	$HCO+OH \rightarrow CO+H_2O$	1.69E-10	1.69E-10	(Baulch et al., 1992)
cab_{26}	$HCO+O_2 \rightarrow CO+HO_2$	5.20E-12	5.20E-12	(Sander et al., 2011)
cab_{27}	$HCO+H \rightarrow CO+H_2$	1.83E-10	1.83E-10	(Friedrichs et al., 2002)
cab_{28}	$HOCH_2O_2 \rightarrow HCHO+HO_2$	2.40E12exp(-7,000/T)	150.89 [b]	(Sander et al., 2019)
cab_{29}	$HOCH_2O_2+HO_2 \rightarrow 0.5{\ast}HOCH_2OOH$ $+0.5{\ast}HCOOH+0.2{\ast}OH+0.2{\ast}HO_2+0.3{\ast}H_2O+0.8{\ast}O_2$	5.6E-15exp(2,300/T)	1.26E-12	(Sander et al., 2019)
cab_{30}	$HOCH_2O_2+R-O_2 \rightarrow HCOOH+HO_2$	$2 \times (\text{k\_ch3o2} \times 5.50\text{E-}12)^{0.5}$	2.78E-12	(Sander et al., 2019)
cab_{31}	$HOCH_2O_2+R-O_2 \rightarrow 0.5{\ast}HCOOH$ $+0.5{\ast}HOCH_2OH+0.5{\ast}O_2$	$2 \times (\text{k\_ch3o2} \times 5.70\text{E-}14 \times \exp(750/T)\ )^{0.5}$	9.95E-13	(Sander et al., 2019)
cab_{32}	$HCOOH+OH \rightarrow CO_2+HO_2+H_2O$	2.94E-14exp(786/T) + 9.85E-13exp(-1,036/T)	4.42E-13	(Sander et al., 2019)
cab_{33}	$HOCH_2OOH+OH \rightarrow HOCH_2O_2$	k_roohro	6.02E-12	(Sander et al., 2019)
cab_{34}	$HOCH_2OOH+OH \rightarrow HCOOH+H_2O+OH$	k_rohro + k_s × f_soh × f_sooh	2.59E-11	(Sander et al., 2019)
cab_{35}	$HOCH_2OH+OH \rightarrow HO_2+HCOOH+H_2O$	$2 \times \text{k\_rohro} + \text{k\_s} \times \text{f\_soh}^2$	1.13E-11	(Sander et al., 2019)
cab_{107}	$CH_3+OH+M \rightarrow CH_3OH+M$	$2.5 \times \text{dens} \times 2.48\text{E-}27\exp(298./t)^{3.8}$	9.92E-10	(Fagerstrm et al., 1994)

Note. Bimolecular rate coefficient units are $cm^3\ molec^{-1}\ s^{-1}$. [a] are three-body reactions with values taken with atmospheric number density complying to temperatures of T = 298 K and pressures of 660 Pa. [b] are unimolecular rate coefficients with units s^{-1}.

Table B5

Chemical Reactions and Rate Coefficients Involved in the Oxidation of C_2H_6 Used in Our 1-D Photochemistry Model

Ethane reaction scheme

Key	Reaction	Formula	Rate at T = 298 K	Reference
cab$_{36}$	$C_2H_6+OH\rightarrow C_2H_5+H_2O$	7.66E-12exp(-1,020/T)	2.50E-13	(Sander et al., 2011)
cab$_{37}$	$C_2H_6+O\rightarrow C_2H_5+OH$	2.21E-15(T/298)$^{6.5}$exp(-132/T)	1.42E-15	(Cohen & Westberg, 1991)
cab$_{38}$	$CH_3+CH_3+M\rightarrow C_2H_6$	Details in (Cody et al., 2003)	5.12E-11 [a]	(Cody et al., 2003)
cab$_{39}$	$C_2H_5+O_2+M\rightarrow C_2H_5O_2$	2.5 × 1.50E-28(298/T)^3×dens	6.02E-11 [a]	(Sander et al., 2011)
cab$_{40}$	$C_2H_5+C_2H_5\rightarrow C_2H_4+C_2H_6$	2.01E-12	2.01E-12	(Dobis & Benson, 1991)
cab$_{41}$	$C_2H_5+O_2\rightarrow C_2H_4+HO_2$	1.90E-14	1.90E-14	(Sander et al., 2011)
cab$_{42}$	$C_2H_5+H\rightarrow CH_3+CH_3$	7.95E-11exp(-132/T)	5.11E-11	(Pratt & Wood, 1984)
cab$_{43}$	$C_2H_5O_2+HO_2\rightarrow C_2H_5OOH+O_2$	7.50E-13exp(700/T)	7.86E-12	(Sander et al., 2019)
cab$_{44}$	$C_2H_5O_2+RO_2\rightarrow 0.8\ast CH_3CHO+0.6\ast HO_2$ $+0.2\ast C_2H_5OH+O_2$	2(7.60E-14*k_ch3o2)$^{0.5}$	3.27E-13	(Sander et al., 2019)
cab$_{45}$	$C_2H_5OOH+HO_2\rightarrow C_2H_5OOH+O_2$	k_roohro	6.02E-12	(Sander et al., 2019)
cab$_{46}$	$C_2H_5OOH+OH\rightarrow CH_3CHO+OH$	k_s*f_sooh	7.47E-12	(Sander et al., 2019)
cab$_{47}$	$C_2H_5OH+OH\rightarrow 0.95\ast C_2H_5O_2+0.95\ast HO_2$ $+0.05\ast HOCH_2CH_2O_2+H_2O$	3.00E-12exp(20/T)	3.21E-12	(Sander et al., 2019)
cab$_{48}$	$HOCH_2CH_2O_2+RO_2\rightarrow 0.6\ast HOCH_2CH_2O$ $+0.2\ast HOCH_2CHO+0.2\ast ETHGLY$	2*(7.80E-14exp(1,000/T)*k_ch3o2)$^{0.5}$	1.77E-12	(Sander et al., 2019)
cab$_{49}$	$HOCH_2CH_2O_2+HO_2\rightarrow HYETHO2H$	1.53E-13exp(1300/T)*(1-k_rchohch2o2_oh)	1.08E-11	(Sander et al., 2019)
cab$_{50}$	$HOCH_2CH_2O_2+HO_2\rightarrow HOCH_2CH_2O+OH$	1.53E-13exp(1300/T)*k_rchohch2o2_oh	1.20E-12	(Sander et al., 2019)
cab$_{51}$	$HOCH_2CH_2O+O_2\rightarrow HO_2+HOCH_2CHO$	6.00E-14exp(-550/T)	9.48E-15	(Sander et al., 2019)
cab$_{52}$	$HOCH_2CH_2O\rightarrow HO_2+HCHO+HCHO$	9.5E13exp(-5,988/T)	1.78E5 [b]	(Sander et al., 2019)
cab$_{53}$	$ETHGLY+OH\rightarrow HOCH_2CHO+HO_2+H_2O$	2*k_s*f_soh*f_pch2oh + 2*k_rohro	8.57E-12	(Sander et al., 2019)
cab$_{54}$	$HYETHO2H+OH\rightarrow HOCH_2CH_2O_2+H_2O$	k_roohro	6.02E-12	(Sander et al., 2019)
cab$_{55}$	$HYETHO2H+OH\rightarrow HOCH_2CHO+OH+H_2O$	k_s*f_sooh*f_pch2oh	9.64E-12	(Sander et al., 2019)
cab$_{56}$	$HYETHO2H+OH\rightarrow HOOCH_2CHO+HO_2+H_2O$	k_s*f_soh*f_pch2oh + k_rohro	4.29E-12	(Sander et al., 2019)
cab$_{57}$	$CH_3CHO+OH\rightarrow CH_3C(O)+H_2O$	4.40E-12exp(365/T)*0.95	1.42E-11	(Sander et al., 2019)
cab$_{58}$	$CH_3CHO+OH\rightarrow HCOCH_2O_2+H_2O$	4.40E-12exp(365/T)*0.05	7.48e-13	(Sander et al., 2019)
cab$_{59}$	$CH_3CHO+HO_2\rightarrow CH_3CHOHO_2$	3.46E12exp(-12,500/(1.98*T)) / 6.34E26*exp(-1,470/(1.98*T))	4.77E-22	(Sander et al., 2019)
cab$_{60}$	$CH_3CHO+HCOOH\rightarrow CH_2CHOH+HCOOH$	(1.17E-19*T$^{2.209}$)exp(-556/(1.987T))	1.34E-14	(Sander et al., 2019)
cab$_{61}$	$CH_2CHOH+OH\rightarrow HCOOH+OH+HCHO$	4.30E-11	4.30E-11	(Sander et al., 2019)
cab$_{62}$	$CH_2CHOH+OH\rightarrow HOCH_2CHO+HO_2$	2.40E-11	2.40E-11	(Sander et al., 2019)
cab$_{63}$	$CH_2CHOH+HCOOH\rightarrow CH_3CHO+HCOOH$	(4.67E-26*T$^{3.286}$)exp(-556/(T*1.987))	2.47E-18	(Sander et al., 2019)
cab$_{64}$	$CH_3CHOHO_2\rightarrow CH_3CHO+HO_2$	3.46E12exp(-12,500/(T*1.98))	2.18E3 [b]	(Sander et al., 2019)
cab$_{65}$	$CH_3CHOHO_2+HO_2\rightarrow 0.5\ast CH_3CHOHOOH$ $+0.3\ast CH_3COOH+0.2\ast CH_3+0.2\ast HCOOH+0.2\ast OH$ $+O_2$	5.60E-15exp(2300/T)	1.26E-11	(Sander et al., 2019)
cab$_{66}$	$CH_3CHOHO_2+RO_2\rightarrow CH_3+HCOOH+OH$	k_ro2soro2	9.68E-13	(Sander et al., 2019)
cab$_{67}$	$CH_3COOH+OH\rightarrow CH_3+CO_2+H_2O$	4.00E-14exp(850/T)	6.93E-13	(Sander et al., 2019)
cab$_{68}$	$CH_3CHOHOOH+OH\rightarrow CH_3COOH+OH$	k_t*f_tooh*f_toh + k_rohro	4.19E-11	(Sander et al., 2019)
cab$_{69}$	$CH_3CHOHOOH+OH\rightarrow CH_3CHOHO_2$	k_roohro	6.02E-12	(Sander et al., 2019)
cab$_{70}$	$CH_3C(O)+O_2+M\rightarrow CH_3C(O)OO+M$	5.10E-12(1 - 1/(1 + 9.48E-18*dens*2.5))	4.04E-12 [a]	(Sander et al., 2019)
cab$_{71}$	$CH_3C(O)+O_2+M\rightarrow OH+HCHO+CO+M$	5.10E-12/(1 + 9.48E-18*dens*2.5))	1.06E-12 [a]	(Sander et al., 2019)
cab$_{72}$	$CH_3C(O)OO+HO_2\rightarrow OH+CH_3+CO_2$	5.20E-13exp(980/T)*1.507*0.61	1.28E-11	(Sander et al., 2019)
cab$_{73}$	$CH_3C(O)OO+HO_2\rightarrow CH_3C(O)OOH$	5.20E-13exp(980/T)*1.507*0.23	4.83E-12	(Sander et al., 2019)
cab$_{74}$	$CH_3C(O)OO+HO_2\rightarrow CH_3COOH+O_3$	5.20E-13exp(980/T)*1.507*0.16	3.36E-12	(Sander et al., 2019)
cab$_{75}$	$CH_3C(O)OO+RO_2\rightarrow CH_3+CO_2$	k_ro2rco3*0.9	1.93E-11	(Sander et al., 2019)
cab$_{76}$	$CH_3C(O)OO+RO_2\rightarrow CH_3COOH$	k_ro2co3*0.1	2.14E-12	(Sander et al., 2019)
cab$_{77}$	$CH_3C(O)OOH+OH\rightarrow CH_3C(O)OO+H_2O$	k_roohro	6.02E-12	(Sander et al., 2019)
cab$_{78}$	$HCOCH_2O_2+RO_2\rightarrow 0.6\ast HCHO+0.6\ast CO+0.6\ast HO_2$ $+0.2\ast GLYOX+0.2\ast HOCH_2CHO$	k_ro2poro2	8.03E-12	(Sander et al., 2019)
cab$_{79}$	$HCOCH_2O_2+HO_2\rightarrow HOOCH_2CHO$	k_ro2ho2_2*rcoch2o2_ooh	7.52E-12	(Sander et al., 2019)
cab$_{80}$	$HCOCH_2O_2+HO_2\rightarrow HCHO+CO+HO_2+OH$	k_ro2ho2_2*rcoch2o2_oh	1.33E-12	(Sander et al., 2019)
cab$_{81}$	$GLYOX+OH\rightarrow HCOCO+H_2O$	3.10E-12exp(340/T)	9.70E-12	(Sander et al., 2019)
cab$_{82}$	$HCOCO\rightarrow HCO+CO$	1.40E12exp(-3,159/T)	3.54E7 [b]	(Orlando & Tyndall, 2001)
cab$_{83}$	$HCOCO+O_2\rightarrow HCOCO_3$	5.00E-12*3.2*exp(-550/T)	2.53E-12	(Sander et al., 2019)

Table B5
Continued

Ethane reaction scheme

cab_{84}	$HCOCO+O_2 \rightarrow OH+CO+CO_2$	5.00E-12(1 - 3.2exp(-550/T))	2.47E-12	(Sander et al., 2019)
cab_{85}	$HOOCH_2CHO+OH \rightarrow HCOCH_2O_2+H_2O$	k_roohro	6.02E-12	(Sander et al., 2019)
cab_{86}	$HOOCH_2CHO+OH \rightarrow HCHO+CO+OH+H_2O$	0.8*8.00E-12	6.40E-12	(Sander et al., 2019)
cab_{87}	$HOOCH_2CHO+OH \rightarrow GLYOX+OH+H_2O$	0.55*k_s*f_sooh*f_cho	2.26E-12	(Sander et al., 2019)
cab_{88}	$HOCH_2CHO+OH \rightarrow HOCH_2CO+H_2O$	0.8*8.00E-12	6.40E-12	(Sander et al., 2019)
cab_{89}	$HOCH_2CHO+OH \rightarrow HOCHCHO+H_2O$	0.2*8.00E-12	1.60E-12	(Sander et al., 2019)
cab_{90}	$HOCHCHO \rightarrow GLYOX+HO_2$	kdec	1.00E6 [b]	(Sander et al., 2019)
cab_{91}	$HOCH_2CO+O_2+M \rightarrow HOCH_2CO_3+M$	5.10E-12*(1 - 1/(1 + 1.85E-18*dens*2.5))	2.17E-12 [a]	(Sander et al., 2019)
cab_{92}	$HOCH_2CO+O_2+M \rightarrow OH+HCHO+CO_2+M$	5.10E-12*(1 + 1.85E-18*dens*2.5)	8.89E-12 [a]	(Sander et al., 2019)
cab_{93}	$HOCH_2CO_3+RO_2 \rightarrow HCHO+CO_2+HO_2$	k_ro2rco3*0.9	1.93E-11	(Sander et al., 2019)
cab_{94}	$HOCH_2CO_3+RO_2 \rightarrow HOCH_2CO_2H$	k_ro2rco3*0.1	2.14E-12	(Sander et al., 2019)
cab_{95}	$HOCH_2CO_3+HO_2 \rightarrow HCHO+OH+HO_2+CO_2$	kapho2*rco3_oh	9.25E-12	(Sander et al., 2019)
cab_{96}	$HOCH_2CO_3+HO_2 \rightarrow HOCH_2CO_3H$	kapho2*rco3_ooh	2.82E-12	(Sander et al., 2019)
cab_{97}	$HOCH_2CO_3+HO_2 \rightarrow HOCH_2CO_2H+O_3$	kapho2*rco3_o3	1.34E-12	(Sander et al., 2019)
cab_{98}	$HOCH_2CO_2H+OH \rightarrow 0.09 \ast HCHO+0.91 \ast HCOCO_2H +HO_2+H_2O$	k_co2h + k_s*f_soh*f_co2h	5.50E012	(Sander et al., 2019)
cab_{99}	$HCOCO_2H+OH \rightarrow CO+HO_2+CO_2+H_2O$	k_co2h + k_t*f_o*f_co2h	2.66E-11	(Sander et al., 2019)
cab_{100}	$HOCH_2CO_3H+OH \rightarrow HOCH_2CO_3+H_2O$	k_roohro	6.02E-12	(Sander et al., 2019)
cab_{101}	$HOCH_2CO_3H+OH \rightarrow HCOCO_3H+HO_2$	k_s*f_soh*f_co2h	5.37E-12	(Sander et al., 2019)
cab_{102}	$HCOCO_3H+OH \rightarrow HCOCO_3+H_2O$	k_roohro	6.02E-12	(Sander et al., 2019)
cab_{103}	$HCOCO_3H+OH \rightarrow CO+CO_2+H_2O+OH$	k_t*f_o*f_co2h	2.65E-11	(Sander et al., 2019)
cab_{104}	$HCOCO_3+RO_2 \rightarrow CO+HO_2+CO_2$	k_ro2rco3*0.9	1.93E-11	(Sander et al., 2019)
cab_{105}	$HCOCO_3+RO_2 \rightarrow HCOCO_2H+O_2$	k_ro2rco3*0.1	2.14E-12	(Sander et al., 2019)
cab_{106}	$HCOCO_3+HO_2 \rightarrow HO_2+CO+CO_2+OH$	kapho2	1.34E-11	(Sander et al., 2019)

Note. Bimolecular rate coefficient units are cm^3 molec^{-1} s^{-1}. [a] are three-body reactions with values taken with atmospheric number density complying to temperatures of T = 298 K and pressures of 660 Pa. [b] are unimolecular rate coefficients with units s^{-1}.

Table B6
Organic Photolytic Reactions Used Within the 1-D Photochemistry Submodule

Key	Reaction	J(z = 0.50 km)	J(z = 42.67 km)	J(z = 69.81 km)
$j_{CH_4 \rightarrow CH_3}$	$CH_4+h\nu \rightarrow CH_3+H$	0.00	0.00	8.12E-10
$j_{CH_4 \rightarrow {}^1CH_2}$	$CH_4+h\nu \rightarrow {}^1CH_2+H_2$	0.00	0.00	1.63E-9
$j_{CH_4 \rightarrow {}^3CH_2}$	$CH_4+h\nu \rightarrow {}^3CH_2+H+H$	0.00	0.00	1.53E-10
$j_{CH_4 \rightarrow CH}$	$CH_4+h\nu \rightarrow CH+H_2+H$	0.00	0.00	1.95E-10
j_{CH_3OOH}	$CH_3OOH+h\nu \rightarrow CH_3O+OH$	2.23E-5	2.90E-5	2.97E-5
$j_{HCHO \rightarrow HCO}$	$HCHO+h\nu \rightarrow HCO+H$	3.54E-5	4.62E-5	4.74E-5
$j_{HCHO \rightarrow CO}$	$HCHO+h\nu \rightarrow H_2+CO$	3.71E-5	4.88E-5	5.01E-5
j_{CH_3OH}	$CH_3OH+h\nu \rightarrow CH_3O+H$	1.59E-7	1.12E-6	1.64E-6
$j_{C_2H_6}$	$C_2H_6+h\nu \rightarrow Products$	0.00	0.00	2.39E-9
$j_{CH_3CHO \rightarrow CH_3}$	$CH_3CHO+h\nu \rightarrow CH_3+HCO$	2.43E-5	3.40E-5	3.44E-5
$j_{CH_3CHO \rightarrow CH_4}$	$CH_3CHO+h\nu \rightarrow CH_4+CO$	5.46E-6	6.80E-6	6.81E-6
j_{HOCH_2OOH}	$HOCH_2OOH+h\nu(+O_2) \rightarrow HCOOH +HO_2+OH$	4.43E-5	5.43E-5	5.43E-5
$j_{HOCH_2CHO \rightarrow HCO}$	$HOCH_2CHO+h\nu \rightarrow CH_3O+HCO$	4.08E-5	5.04E-5	5.05E-5
$j_{HOCH_2CHO \rightarrow CO}$	$HOCH_2CHO+h\nu \rightarrow CH_3OH+CO$	4.91E-6	6.07E-6	6.09E-6
$j_{HOCH_2CHO \rightarrow OH}$	$HOCH_2CHO+h\nu(+O_2) \rightarrow HCOCH_2O_2+OH$	3.44E-6	4.25E-6	4.26E-6

Table B6
Continued

Key	Reaction	J(z = 0.50 km)	J(z = 42.67 km)	J(z = 69.81 km)
$j_{Glyox \rightarrow HCO}$	$Glyoxal+h\nu \rightarrow HCO+HCO$	7.84E-5	8.49E-5	8.5E-5
$j_{Glyox \rightarrow H_2}$	$Glyoxal+h\nu \rightarrow H_2+CO+CO$	1.90E-5	2.19E-5	2.20E-5
$j_{Glyox \rightarrow HCHO}$	$Glyoxal+h\nu \rightarrow HCHO+CO$	2.79E-5	3.13E-5	3.14E-5
j_{CH_3COOH}	$CH_3COOH+h\nu \rightarrow CH_3+COOH$	7.77E-6	9.43E-6	9.44E-6
$j_{CH_3C(O)OOH}$	$CH_3C(O)OOH+h\nu \rightarrow CH_3+OH+CO_2$	3.85E-5	4.73E-6	4.75E-5
Proxies				
Key	Reaction	Proxy	Source	
$j_{HOCH_2CO_3H}$	$HOCH_2CO_3H+h\nu \rightarrow HCHO+HO2+OH+CO2$	j_{CH_3OOH}	(Sander et al., 2014)	
j_{HCOCO_2H}	$HCOCO_2H+h\nu \rightarrow 2HO_2+CO+CO_2$	$3.95 \times j_{HCHO \rightarrow CO}$	(Kuhlmann et al., 2003)	
$j_{CH_3CHOHOOH}$	$CH_3CHOHOOH+h\nu \rightarrow CH_3+HCOOH+OH$	j_{CH_3OOH}	(Sander et al., 2014)	
$j_{Hyetho2h}$	$Hyetho2h+h\nu \rightarrow HO_2+CO+OH+CO_2$	$j_{CH_3OOH}+j_{HOCH_2CHO \rightarrow HCO}+j_{HOCH_2CHO \rightarrow CO}+j_{HOCH_2CHO \rightarrow OH}$	(Sander et al., 2014)	
j_{HCOCO_3H}	$HCOCO_3H+h\nu \rightarrow HO_2+CO+OH+CO2$	$j_{Hyetho2h}$	(Sander et al., 2014)	
j_{HOOCH_2CHO}	$HOOCH_2CHO+h\nu \rightarrow HCHO+OH+HO2+CO$	$j_{Hyetho2h}$	(Sander et al., 2014)	

Note. Values (s^{-1}) are interpolated from an offline look-up table constructed by a modified TUV (Madronich et al., 2002) model with respect to CO_2 and O_3 column abundances overheard, temperature, optical opacity and solar zenith angle. Values displayed are extracted for a solar zenith angle of 0°, L_S = 251° (perihelion).

Acknowledgments

We gratefully acknowledge Stephen Lewis for providing the 1-D atmospheric chemistry sub-module of the LMD-UK MGCM. We also thank Manish Patel for providing insights into Trace Gas Orbiter instruments and thank Rolf Sander for maintaining the CAABA/MECCA Box model, published under the GNU GPL, which we have used to develop our description of Mars' photochemistry. We thank Sasha Madronich and the National Center for Atmospheric Research for providing the source code of the Tropospheric and Ultraviolet Radiation model used to construct the offline look-up table of photolysis rates of organic compounds that the 1-D model interpolates from. B. M.T. acknowledges his PhD studentship funding (ST/1/R001324/1) from the UK Space Agency, administered by the Science and Technology Facilities Council, as part of the Aurora science programme.

References

Atkinson, R., Baulch, D. L., Cox, R. A., Crowley, J. N., Hampson, R. F., Hynes, R. G., et al. (2006). Evaluated kinetic and photochemical data for atmospheric chemistry: Volume ii; gas phase reactions of organic species. *Atmospheric Chemistry and Physics*, *6*(11), 3625–4055. https://doi.org/10.5194/acp-6-3625-2006

Baulch, D. L., Bowman, C. T., Cobos, C. J., Cox, R. A., Just, T., Kerr, J. A., et al. (2005). Evaluated kinetic data for combustion modeling: Supplement ii. *Journal of Physical and Chemical Reference Data*, *34*(3), 757–1397. https://doi.org/10.1063/1.1748524

Baulch, D. L., Cobos, C. J., Cox, R. A., Esser, C., Frank, P., Just, T., et al. (1992). Evaluated kinetic data for combustion modelling. *Journal of Physical and Chemical Reference Data*, *21*(3), 411–734. https://doi.org/10.1063/1.555908

Campbell, I. M., & Gray, C. N. (1973). Rate constants for o(3p) recombination and association with n(4s). *Chemical Physics Letters*, *18*(4), 607–609. https://doi.org/10.1016/0009-2614(73)80479-8

Christensen, L. E., Okumura, M., Sander, S. P., Salawitch, R. J., Toon, G. C., Sen, B., et al. (2002). Kinetics of ho2 + ho2 h2o2 + o2: Implications for stratospheric h2o2. *Geophysical Research Letters*, *29*(9), 2002. https://doi.org/10.1029/2001GL014525

Cody, R. J., Romani, P. N., Nesbitt, F. L., Iannone, M. A., Tardy, D. C., & Stief, L. J. (2003). Rate constant for the reaction ch3 + ch3 c2h6 at t = 155 k and model calculation of the ch3 abundance in the atmospheres of saturn and neptune. *Journal of Geophysical Research*, *108*, 5119. https://doi.org/10.1029/2002JE002037

Cohen, N., & Westberg, K. R. (1991). Chemical kinetic data sheets for high temperature reactions. part ii. *Journal of Physical and Chemical Reference Data*, *20*(6), 1211–1311. https://doi.org/10.1063/1.555901

Dobis, O., & Benson, S. W. (1991). Temperature coefficients of the rates of chlorine atom reactions with c2h6, c2h5, and c2h4. the rates of disproportionation and recombination of ethyl radicals. *Journal of the American Chemical Society*, *113*(17), 6377–6386. https://doi.org/10.1021/ja00017a004

Fagerstrm, K., Lund, A., Mahmoud, G., Jodkowski, J. T., & Ratajczak, E. (1994). Pressure and temperature dependence of the gas-phase reaction between methyl and hydroxyl radicals. *Chemical Physics Letters*, *224*(1), 43–50. https://doi.org/10.1016/0009-2614(94)00513-3

Fedorova, A., Korablev, O., Bertaux, J.-L., Rodin, A., Kiselev, A., & Perrier, S. (2006). Mars water vapor abundance from spicam ir spectrometer: Seasonal and geographic distributions. *Journal of Geophysical Research*, *111*, E09S08. https://doi.org/10.1029/2006JE002695

Fonti, S., & Marzo, G. A. (2010). Mapping the methane on Mars. *Astronomy and Astrophysics*, *512*, A51. https://doi.org/10.1051/0004-6361/200913178

Forget, F., Hourdin, F., Fournier, R., Hourdin, C., Talagrand, O., Collins, M., et al. (1999). Improved general circulation models of the Martian atmosphere from the surface to above 80 km. *Journal of Geophysics Research*, *104*, 24,155–24,176. https://doi.org/10.1029/1999JE001025

Forget, F., Hourdin, F., & Talagrand, O. (1998). CO $_2$Snowfall on Mars: Simulation with a General Circulation Model. *Icarus*, *131*, 302–316. https://doi.org/10.1006/icar.1997.5874

Formisano, V., Angrilli, F., Arnold, G., Atreya, S., Bianchini, G., Biondi, D., et al. (2005). The planetary fourier spectrometer (pfs) onboard the european mars express mission. *Planetary and Space Science*, *53*(10), 963–974. https://doi.org/10.1016/j.pss.2004.12.006

Formisano, V., Atreya, S., Encrenaz, T., Ignatiev, N., & Giuranna, M. (2004). Detection of methane in the atmosphere of mars. *Science*, *306*(5702), 1758–1761. https://doi.org/10.1126/science.1101732

Friedrichs, G., Herbon, J. T., Davidson, D. F., & Hanson, R. K. (2002). Quantitative detection of hco behind shock waves: The thermal decomposition of hco. *Physical Chemistry Chemical Physics*, *4*, 5778–5788. https://doi.org/10.1039/B205692E

Geminale, A., Formisano, V., & Giuranna, M. (2008). Methane in martian atmosphere: Average spatial, diurnal, and seasonal behaviour. *Planetary and Space Science*, *56*(9), 1194–1203. https://doi.org/10.1016/j.pss.2008.03.004

Geminale, A., Formisano, V., & Sindoni, G. (2011). Mapping methane in martian atmosphere with pfs-mex data. *Planetary and Space Science*, *59*(2), 137–148. https://doi.org/10.1016/j.pss.2010.07.011

Giuranna, M., Viscardy, S., Daerden, F., Neary, L., Etiope, G., Oehler, D., et al.(2019). Independent confirmation of a methane spike on mars and a source region east of gale crater. *Nature Geoscience*, *12*, 326–332. https://doi.org/10.1038/s41561-019-0331-9

Gordon, I. E., Rothman, L. S., Hill, C., Kochanov, R. V., Tan, Y., Bernath, P. F., et al. (2017). The hitran2016 molecular spectroscopic database. *Journal of Quantitative Spectroscopy and Radiative Transfer*, *203*, 3–69. https://doi.org/10.1016/j.jqsrt.2017.06.038

Groß, C. B. M., Dillon, T. J., Schuster, G., Lelieveld, J., & Crowley, J. N. (2014). Direct kinetic study of oh and o3 formation in the reaction of ch3c(o)o2 with ho2. *The Journal of Physical Chemistry A*, *118*(6), 974–985. https://doi.org/10.1021/jp412380z

Guenther, A., Geron, C., Pierce, T., Lamb, B., Harley, P., & Fall, R. (2000). Natural emissions of non-methane volatile organic compounds, carbon monoxide, and oxides of nitrogen from north america. *Atmospheric Environment*, *34*(12), 2205–2230. https://doi.org/10.1016/S1352-2310(99)00465-3

Herron, J. T. (1988). Evaluated chemical kinetic data for the reactions of atomic oxygen o(3p) with saturated organic compounds in the gas phase. *Journal of Physical and Chemical Reference Data*, *17*(3), 967–1026. https://doi.org/10.1063/1.555810

Horita, J., & Berndt, M. E. (1999). Abiogenic methane formation and isotopic fractionation under hydrothermal conditions. *Science*, *285*(5430), 1055–1057. https://doi.org/10.1126/science.285.5430.1055

Joshi, A. V., & Wang, H. (2006). Master equation modeling of wide range temperature and pressure dependence of co + oh products. *International Journal of Chemical Kinetics*, *38*(1), 57–73. https://doi.org/10.1002/kin.20137

Kaufman, F., & Kelso, J. R. (1967). M effect in the gas phase recombination of o with o2. *The Journal of Chemical Physics*, *46*(11), 4541–4543. https://doi.org/10.1063/1.1840589

Korablev, O., Montmessin, F., Trokhimovskiy, A., Fedorova, A. A., Shakun, A. V., Grigoriev, A. V., et al. (2017). The atmospheric chemistry suite (acs) of three spectrometers for the exomars 2016 trace gas orbiter. *Space Science Reviews*, *214*(1), 7. https://doi.org/10.1007/s11214-017-0437-6

Korablev, O., Vandaele, A. C., Montmessin, F., Fedorova, A. A., Trokhimovskiy, A., Forget, F., et al. (2019). No detection of methane on Mars from early ExoMars Trace Gas Orbiter observations. *Nature*, *568*(7753), 517–520. https://doi.org/10.1038/s41586-019-1096-4

Krasnopolsky, V. A. (2006). Some problems related to the origin of methane on mars. *Icarus*, *180*(2), 359–367. https://doi.org/10.1016/j.icarus.2005.10.015

Krasnopolsky, V. A. (2007). Long-term spectroscopic observations of mars using irtf/cshell: Mapping of o2 dayglow, co, and search for ch4. *Icarus*, *190*(1), 93–102. https://doi.org/10.1016/j.icarus.2007.02.014

Krasnopolsky, V. A. (2011). A sensitive search for methane and ethane on Mars. In *Epsc-dps joint meeting 2011*, pp. 49.

Krasnopolsky, V. A. (2012). Search for methane and upper limits to ethane and so2 on mars. *Icarus*, *217*(1), 144–152. https://doi.org/10.1016/j.icarus.2011.10.019

Krasnopolsky, V. A., Bjoraker, G. L., Mumma, M. J., & Jennings, D. E. (1997). High-resolution spectroscopy of mars at 3.7 and 8 m: A sensitive search for h2o2, h2co, hcl, and ch4, and detection of hdo. *Journal of Geophysical Research*, *102*(E3), 6525–6534. https://doi.org/10.1029/96JE03766

Krasnopolsky, V. A., Maillard, J. P., & Owen, T. C. (2004). Detection of methane in the martian atmosphere: Evidence for life?. *Icarus*, *172*(2), 537–547. https://doi.org/10.1016/j.icarus.2004.07.004

Kuhlmann, R., Lawrence, M., Crutzen, P., & Rasch, P. (2003). A model for studies of tropospheric ozone and nonmethane hydrocarbons: Model description and ozone results. *Journal of Geophysical Research*, *108*(D9), 4294. https://doi.org/10.1029/2002JD002893

Lefèvre, F., & Forget, F. (2009). Observed variations of methane on mars unexplained by known atmospheric chemistry and physics. *Nature*, *460*, 720. https://doi.org/10.1038/nature08228

Lefèvre, F., Lebonnois, S., Montmessin, F., & Forget, F. (2004). Three-dimensional modeling of ozone on mars. *Journal of Geophysical Research*, *109*, E07004. https://doi.org/10.1029/2004JE002268

Lewis, S. R., Collins, M., Read, P. L., Forget, F. A., Hourdin, F. A. A., Fournier, R., et al. (1999). A climate database for mars. *Journal of Geophysical Research*, *104*(E10), 24,177–24,194. https://doi.org/10.1029/1999JE001024

Madeleine, J.-B., Forget, F., Millour, E., Montabone, L., & Wolff, M. J. (2011). Revisiting the radiative impact of dust on Mars using the LMD Global Climate Model. *Journal of Geophysical Research*, *116*, E11010. https://doi.org/10.1029/2011JE003855

Madronich, S., Flocke, S., Zeng, J., Petropavlovskikh, I., & Lee-Taylor, J. (2002). Tropospheric ultraviolet and visible (tuv) radiation model. National Center for Atmospheric Research (NCAR), Boulder, CO. Home page at: http://www.acd.ucar.edu/TUV

Mellor, G. L., & Yamada, T. (1982). Development of a turbulence closure model for geophysical fluid problems. *Reviews of Geophysics and Space Physics*, *20*, 851–875. https://doi.org/10.1029/RG020i004p00851

Millour, E., Forget, F., Spiga, A., Vals, M., Zakharov, V., Navarro, T., et al. (2017). The Mars Climate Database (MCD version 5.3). In *Egu general assembly conference abstracts*, *19*, pp. 12,247.

Montabone, L., Forget, F., Millour, E., Wilson, R. J., Lewis, S. R., Cantor, B., et al. (2015). Eight-year climatology of dust optical depth on mars. *Icarus*, *251*, 65–95. https://doi.org/10.1016/j.icarus.2014.12.034

Moores, J. E., King, P. L., Smith, C. L., Martinez, G. M., Newman, C. E., Guzewich, S. D., et al. (2019). The methane diurnal variation and microseepage flux at gale crater, mars as constrained by the exomars trace gas orbiter and curiosity observations. *Geophysical Research Letters*, *46*, 9430–9438. https://doi.org/10.1029/2019GL083800

Mulenko, S. A. (1980). Investigation of the recombination of the hco radical in an atmosphere of argon and helium by the method of internal resonator laser spectroscopy. *Journal of Applied Spectroscopy*, *33*, 688–694.

Mulenko, S. A. (1987). The application of an intracavity laser spectroscopy method for elementary processes study in gas-phase reactions. Revue Roumaine de Physique.

Mumma, M. J., Villanueva, G. L., Novak, R. E., Hewagama, T., Bonev, B. P., DiSanti, M. A., et al. (2009). Strong release of methane on mars in northern summer 2003. *Science*, *323*(5917), 1041–1045. https://doi.org/10.1126/science.1165243

Nair, H., Allen, M., Anbar, A. D., Yung, Y. L., & Clancy, R. T. (1994). A photochemical model of the martian atmosphere. *Icarus*, *111*(1), 124–150. https://doi.org/10.1006/icar.1994.1137

Navarro, T., Madeleine, J.-B., Forget, F., Spiga, A., Millour, E., Montmessin, F., & Määttänen, A.(2014). Global climate modeling of the Martian water cycle with improved microphysics and radiatively active water ice clouds. *Journal of Geophysical Research: Planets*, *119*, 1479–1495. https://doi.org/10.1002/2013JE004550

Orlando, J. J., & Tyndall, G. S. (2001). The atmospheric chemistry of the hc(o)co radical. *International Journal of Chemical Kinetics*, *33*(3), 149–156. https://doi.org/10.1002/1097-4601(200103)33:3<149::AID-KIN1008>3.0.CO;2-1

Pratt, G. L., & Wood, S. W. (1984). Kinetics of the reaction of methyl radicals with oxygen. *Journal of the Chemical Society, Faraday Transactions 1*, *80*, 3419–3427. https://doi.org/10.1039/F19848003419

Robert, S., Vandaele, A. C., Thomas, I., Willame, Y., Daerden, F., Delanoye, S., et al. (2016). Expected performances of the nomad/exomars instrument. *Planetary and Space Science*, *124*, 94–104. https://doi.org/10.1016/j.pss.2016.03.003

Rodrigo, R., Garca-lvarez, E., Lpez-Gonzlez, M. J., & Lpez-Moreno, J. J. (1990). A nonsteady one-dimensional theoretical model of mars' neutral atmospheric composition between 30 and 200 km. *Journal of Geophysical Research*, *95*(B9), 14,795–14,810. https://doi.org/10.1029/JB095iB09p14795

Rosner, B. M., & Schink, B. (1995). Purification and characterization of acetylene hydratase of pelobacter acetylenicus, a tungsten iron-sulfur protein. *Journal of Bacteriology*, *177*, 5767–72. https://doi.org/10.1128/jb.177.20.5767-5772.1995

Sander, S. P., Abbatt, J., Barker, J., Burkholder, J. B., Friedl, R. R., Golden, D. M., et al. (2011). Chemical kinetics and photochemical data for use in atmospheric studies, evaluation no. 17.

Sander, R., Baumgaertner, A., Cabrera-Perez, D., Frank, F., Gromov, S., Grooß, J.-U., et al. (2019). The community atmospheric chemistry box model caaba/mecca-4.0. *Geoscientific Model Development*, *12*(4), 1365–1385. https://doi.org/10.5194/gmd-12-1365-2019

Sander, S., Finlayson-Pitts, B., Friedl, R., Golden, D., Huie, R., Keller-Rudek, H., et al. (2006). Chemical kinetics and photochemical data for use in atmospheric studies. evaluation no. 15 (jpl publication 06-2).

Sander, S., Friedl, R., Golden, D., Kurylo, M., Huie, R., Orkin, V., et al. (2003). Chemical kinetics and photochemical data for use in atmosheric studies; jpl publication 02-25.

Sander, R., Jöckel, P., Kirner, O., Kunert, A., Landgraf, J., Pozzer, A., & Kirner, O. (2014). The photolysis module jval-14, compatible with the messy standard, and the jval preprocessor (jvpp). *Geoscientific Model Development*, *7*, 2653–2662. https://doi.org/10.5194/gmd-7-2653-2014

Summers, M. E., Lieb, J. B., Chapman, E., & Yung, Y. L. (2002). Atmospheric biomarkers of subsurface life on mars. *Geophysical Research Letters*, *29*(24), 2171. https://doi.org/10.1029/2002GL015377

Taraborrelli, D. (2010). Isoprene oxidation and its impacts on the atmospheric composition (Ph.D. Thesis).

Taysum, B. (2020). Output Files of the 1-D Submodule in The Photochemistry of Methane and Ethane in the Martian Atmosphere. https://doi.org/10.5281/zenodo.3824085

Taysum, B. (2020a). bentaysum/1D_model_rebuild: Revised: AGU - Photochemistry of Methane and Ethane in the Martian Atmosphere. https://doi.org/10.5281/zenodo.3824053

Taysum, B. (2020b). Datafiles for the 1-d photochemistry submodule. https://doi.org/10.5281/zenodo.3733208

Tsang, W., & Hampson, R. F. (1986). Chemical kinetic data base for combustion chemistry. part i. methane and related compounds. *Journal of Physical and Chemical Reference Data*, *15*(3), 1087–1279. https://doi.org/10.1063/1.555759

Vago, J., Witasse, O., Svedhem, H., Baglioni, P., Haldemann, A., Gianfiglio, G., et al. (2015). Esa exomars program: The next step in exploring mars. *Solar System Research*, *49*(7), 518–528. https://doi.org/10.1134/S0038094615070199

Vandaele, A. C., Korablev, O., Daerden, F., Aoki, S., Thomas, I. R., Altieri, F., et al. (2019). Martian dust storm impact on atmospheric H_2O and D/H observed by ExoMars Trace Gas Orbiter. *Nature*, *568*(7753), 521–525. https://doi.org/10.1038/s41586-019-1097-3

Vandaele, A. C., Lopez-Moreno, J.-J., Patel, M. R., Bellucci, G., Daerden, F., Ristic, B., et al. (2018). Nomad, an integrated suite of three spectrometers for the exomars trace gas mission: Technical description, science objectives and expected performance. *Space Science Reviews*, *214*(5), 80. https://doi.org/10.1007/s11214-018-0517-2

Veyret, B., Rayez, J. C., & Lesclaux, R. (1982). Mechanism of the photooxidation of formaldehyde studied by flash photolysis of formaldehyde-oxygen-nitric oxide mixtures. *The Journal of Physical Chemistry*, *86*(17), 3424–3430.

Villanueva, G. L., Mumma, M. J., Novak, R. E., Radeva, Y. L., Käufl, H. U., Smette, A., et al. (2013). A sensitive search for organics (ch4, ch3oh, h2co, c2h6, c2h2, c2h4), hydroperoxyl (ho2), nitrogen compounds (n2o, nh3, hcn) and chlorine species (hcl, ch3cl) on mars using ground-based high-resolution infrared spectroscopy. *Icarus*, *223*(1), 11–27. https://doi.org/10.1016/j.icarus.2012.11.013

Webster, C. R., Mahaffy, P. R., Atreya, S. K., Flesch, G. J., & Farley, K. A. (2013). Low upper limit to methane abundance on mars. *Science*, *342*(6156), 355–357. https://doi.org/10.1126/science.1242902

Webster, C. R., Mahaffy, P. R., Atreya, S. K., Flesch, G. J., Mischna, M. A., Meslin, P. Y., et al. (2015). Mars methane detection and variability at gale crater. *Science*, *347*(6220), 415–417. https://doi.org/10.1126/science.1261713

Webster, C. R., Mahaffy, P. R., Atreya, S. K., Moores, J. E., Flesch, G. J., Malespin, C., et al. (2018). Background levels of methane in mars' atmosphere show strong seasonal variations. *Science*, *360*(6393), 1093–1096. https://doi.org/10.1126/science.aaq0131

Wong, A. S., & Atreya, S. K. (2004). Atmospheric photochemistry above possible martian hot spots. *Advances in Space Research*, *33*(12), 2236–2239. https://doi.org/10.1016/S0273-1177(03)00524-6

Wong, A.-S., Atreya, S. K., & Encrenaz, T. (2003). Chemical markers of possible hot spots on mars. *Journal of Geophysical Research*, *108*(E4), 5026. https://doi.org/10.1029/2002JE002003

Zahnle, K., Freedman, R. S., & Catling, D. C. (2011). Is there methane on mars? *Icarus*, *212*(2), 493–503. https://doi.org/10.1016/j.icarus.2010.11.027